DYNAMICS SIMULATION OF HUMAN BOX DELIVERING TASK

By

Paul Davis Owens, B.S.

A Thesis Submitted in Partial Fulfillment of the Requirements

For the Degree of

Master of Science

University of Alaska Fairbanks

May 2018

APPROVED:

Dr. Yujiang Xiang, Committee Chair
Dr. Rorik Peterson, Committee Member
Dr. Cheng-fu Chen, Committee Member
Dr. Rorik Peterson, Chair
Department of Mechanical Engineering
Dr. Doug Goering, Dean
College of Engineering and Mines
Dr. Michael Castellini, *Dean of the Graduate School*

Abstract

The dynamic optimization of a box delivery motion is a complex task. The key component is to achieve an optimized motion associated with the box weight, delivering speed, and location. This thesis addresses one solution for determining the optimal delivery of a box. The delivering task is divided into five subtasks: lifting, transition step, carrying, transition step, and unloading. Each task is simulated independently with appropriate boundary conditions so that they can be stitched together to render a complete delivering task. Each task is formulated as an optimization problem. The design variables are joint angle profiles. For lifting and carrying task, the objective function is the dynamic effort. The unloading task is a byproduct of the lifting task, but done in reverse, starting with holding the box and ending with it at its final position. In contrast, for transition task, the objective function is the combination of dynamic effort and joint discomfort. The various joint parameters are analyzed consisting of joint torque, joint angles, and ground reactive forces. A viable optimization motion is generated from the simulation results. It is also empirically validated. This research holds significance for professions containing heavy box lifting and delivering tasks and would like to reduce the chance of injury.

Table of Contents

List of Figures

List of Tables

Chapter 1 Introduction

1.1 Motivation

Virtual human modeling and simulation has a history of applications in industry for product design and analysis. There is an evolving demand in industry to evaluate the human aspect of designs within the digital environment. Ergonomic delivering is a typical task with many industry applications, such as manual material handling and automotive assembling line operation. However, simulation of a human delivering task proves to be a challenging problem from an analytical and computational point of view. An accurate biomechanical human model needs to be developed from the sciences of anatomy and physiology. The simulation needs to be fast and efficient computationally in an effort to provide real-time implementations. The primary goal of this study is to develop an accurate two-dimensional (2D) skeletal model to predict and analyze dynamic human delivering motion in ergonomic applications. Inverse dynamics optimization will be used to solve the human motion planning problems.

1.2 Objectives

The objectives of this research can be divided into three aspects. First, inverse dynamics optimization is used to solve a 2D human delivering motion planning problem without integration of the equations of motion. In this approach, an energy-based objective function is chosen based on the minimal energy principle of the motion. Constraints are constructed based on the available information of the bio-system, including physical constraints and task-based constraints. The delivering task is further divided into three sub-tasks: lifting, carrying, and transition between lifting and carrying. Additional subtasks include the transition from walking to standing, and unloading, however these are the reverse of the previous tasks with varied boundary conditions. By combining these sub-tasks, a complete delivering simulation is obtained using optimization.

The second objective is to use the proposed 2D model to predict and analyze lifting and carrying motion. An external load, such as the weight of a box, is discussed by using the proposed predictive models.

Finally, the transition task between lifting and carrying is formulated as an optimization problem. In this formulation, continuity constraints are imposed to connect the lifting and carrying motions into a fluid delivery simulation. In addition, there will be a video-based validation of the complete delivering task for comparative purposes.

The secondary transition from walking to standing and unloading are not unique tasks. They are, however, byproducts of the earlier transition and lifting tasks. The unloading task will follow the same optimization formulation for lifting, with varied initial and final positions.

1.3 Background

There is extensive literature on the study of lifting motion, but only few studies have been done on the delivering task. Here is a brief review of the literature for lifting, carrying, and delivering tasks.

The task of lifting is commonly broken into two different prediction methods: optimization-based and index-based approaches. The optimization-based method can be further broken down to static and dynamic lifting optimization. Noone and Mazumdar [14] used a simple geometrical model to analyze static lifting to determine and compare with other various objective functions. They came to the conclusion that muscle intensity may be a more efficient objective function to determine the optimal lifting motion. Dysart and Woldstad [7] analyzed three objective functions to determine the optimal lifting posture. They concluded that while all three had prevalent prediction errors, minimizing the overall effort yielded the closest similarity to their subject based validation. In addition, the relative height position of the hands played a role in accuracy. Jomoah [12] analyzed a 2D static biomechanical model to calculate the stresses on major joints, as well as the effects of load and lifting technique on the spine during lifting. The conclusion was that a good correlation existed between the inputs of height, weight, and the compressive and shear forces on spine.

Hsiang and McGorry [11] used an optimization approach by minimizing or maximizing different variables to create three distinct dynamic lifting patterns. The three objective functions were: to maximize the smoothness of the lifting motion, to minimize any sudden variance in the center of gravity of the lifter, and to minimize the integration of the sum of the square of the predicted joint moments. Analyzing the compressive forces on the spinal joints from motion pattern of the load, they determined that the peak forces were at the minimum when load took the smoothest path.

Gazula, et al. [9] studied a load-tossing activity, an extension from lifting. The process was broken into three phases, with the goal to determine the relationships between the different objective functions during the tossing process using measured values. In the end, it was determined that no significant correlation exists between the first two phases, however torque utilization and mobilization were important factors in the final phase of tossing.

For lifting, the common method is an optimization-based approach to minimize certain predetermined objective functions. Eberhar and Schiehlen [8] present a review article on the history, formalisms, and applications of modeling multibody dynamics, including the expansion of the field from rigid body to elastic or flexible systems. In addition to history, the article provides an introduction into the variety of methods used to analyze multibody dynamics amongst various fields of research.

Xiang et al. [19] analyzed four different objective functions when studying lifting. The lifting motion was generated from the minimization of the individual functions. The four functions investigated were: dynamic effort, balance criterion, maximum shear force at spine joint, and maximum pressure force at spine joint. As expected each objective function yielded a different lifting motion depending upon its desired result. Ultimately, the dynamic effort performance yielded a squat-like lift, whereas balance criterion and shear at the spine joint illustrated more of a back lift. In addition, the location of the box that was lifted was investigated for its effect on the lifting motions.

Xiang et al. [21] aggregated two objective functions to analyze a multi-objective optimization. The

two functions in play were dynamic effort and stability, and a weighted sum approach was used to combine the two functions, with an enumeration method to determine each of their respective weighing coefficients. The advantages of this methodology are to better understand which functions govern movements with different lifting strategies, and finding the balance between multi-objective functions, creating more natural lifting motion profiles. Ultimately, the program is successful with validation from experimental data.

The basis for carrying is rooted in walking. Currently, there is plenty of research that goes into depth of techniques of simulating and optimizing walking of a bipedal model. Chevallereau and Aoustin [4] studied the optimal gait cycles of a bipedal robot for both running and walking. Bessonnet et al. [2] studied the dynamic-based optimization of sagittal gait cycles, focusing particularly on double-support phases of walking. Rostami and Bessonnet [15] looked at the impact during singles support phases, determining highest instability from the sagittal plane. Sardain and Bessonnet [16] analyzed zero-moment point and walking/running on uneven ground, and the resulting dynamics. Winter [17] analyzed the balance criteria for standing and walking. The study uses an inverted pendulum model to illustrate the reactive components of balancing, and which parts of the body play the largest respective roles. Xiang, et al. [20] determined a general walking optimization for a 3D model studying two transitions: walking to standing and slow to fast walking. All of these researchers studied walking using similar approaches, many using transition matrices determined via the Denavit-Hartenberg [6] method.

Robotics is often an inspiration for a skeletal analysis of walking and balancing for biomechanical purposes. Chung et al. [5] analyzed a 3D skeletal model using human performance measures as an exoskeleton robot design. Similar to other research, the objective functions were minimized in the optimization formulation. In this research, they used an algorithm based on sequential quadratic programing to solve the non-linear optimization problem. The research validated this approach as an assessment tool. Leylavi and Abdei [13] used a simplified approach, looking at a 2D skeleton with seven degrees of freedom, to simulate the lifting (squat like) motion. Looking at two different velocities of lifting, the results showed body posture variance for the two cases to remain balanced.

Anderson and Pandy [1] discussed a simulation of a 3D neuromuscularsketal model combined with dynamic optimization to analyze walking. In their research, they focused more on the muscular excitation and used in relation to metabolic energy expenditure. The energy used was determined by a sum of five sources of energy production. Significantly, the model was assumed symmetric, whereas the left mirrored the right, for simplification of the processes. Validated quantitatively, they determined that the viability of minimum metabolic energy per unit distance traveled as a viable measure of walking performance.

Most every step of the delivery process has been solved a multitude of ways. What there is not research on is how to bridge the steps. In addition, a complete delivery task can be lengthy and computationally strenuous. The objective at hand is to create a program that can generate motion from start to finish of a delivery task. The application of such a simulation is more accurate and complete than the single components of any individual task, and thus more versatile. In addition, it is desirable to make it viable to solve the system without excessive computing power.

1.4 Overview of Thesis and Specific Contributions

The thesis is organized as follows: In Chapter 2, a two-dimensional human skeletal model that has 14 degrees of freedom is built based on the DH method. In addition, the anthropometric data are given for the 2D skeletal model. In Chapter 3, recursive kinematics and dynamics with sensitivity analysis are developed. In Chapters 4 and 5, lifting and carrying are simulated respectively. The effects of box weight and walking speed on the motion are studied. Chapter 6 covers the details of the complete delivering task is simulated by connecting the lifting and carrying together by a transition task. Finally, the thesis ends with Chapter 7 having conclusions and plan of future research.

The research contributions of this work are summarized as follows:

(1) The inverse dynamics optimization method was used to simulate lifting and carrying motions with a 2D skeletal human model. In addition, the transition motion is formulated as an optimization problem to connect lifting and carrying. Therefore, a complete delivering task was simulated for ergonomic analysis.

(2) Joint actuating torque was calculated from the inverse recursive Lagrangian dynamics with analytical gradient evaluations in the optimization process so that the formulation was computationally efficient.

(3) The box weight effects on delivering were studied, and the speed effect on carrying motion was also investigated by using the inverse dynamics optimization method.

Chapter 2 Skeletal Human Modeling

2.1 Two-dimensional Skeletal Model

The skeletal model of this work is defined in the joint space with 14 DOF. Three DOF are used for global translation and rotation and 11 DOF are used for the kinematics of the body as shown in Figure 2.1. In Figure 2.1 the L terms represent the links creating the model, and the z terms represent the joints. The model consists of three physical branches and one virtual branch including the global DOF. The physical branches include the right leg, left leg, spine, and arm. This model is developed by using the Denavit-Hartenberg [6] (DH) method. The anthropometric data for the skeletal model representing a 50th percentile male are generated using GEBOD [3] software.

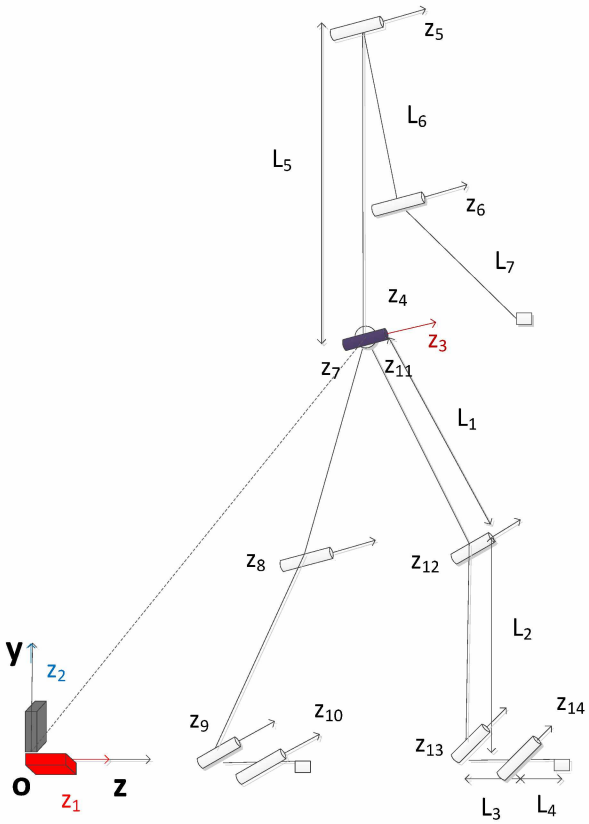

Figure 2.1 The 2D skeletal model

2.2 Denavit-Hartenberg Table

In general, human locomotion means the body moves around. In other words, the global degrees of freedom exist with respect to an inertial reference frame in the mathematical sense. The global degrees of freedom are composed of two translational (prismatic) joints and one rotational (revolute) joints. Figure 2.2 depicts how the global degrees of freedom - global translation (GT) and global rotation (GR) - are set up in the DH method. The degree of freedom is given in the z-direction in both the translational joint and the rotational joint.

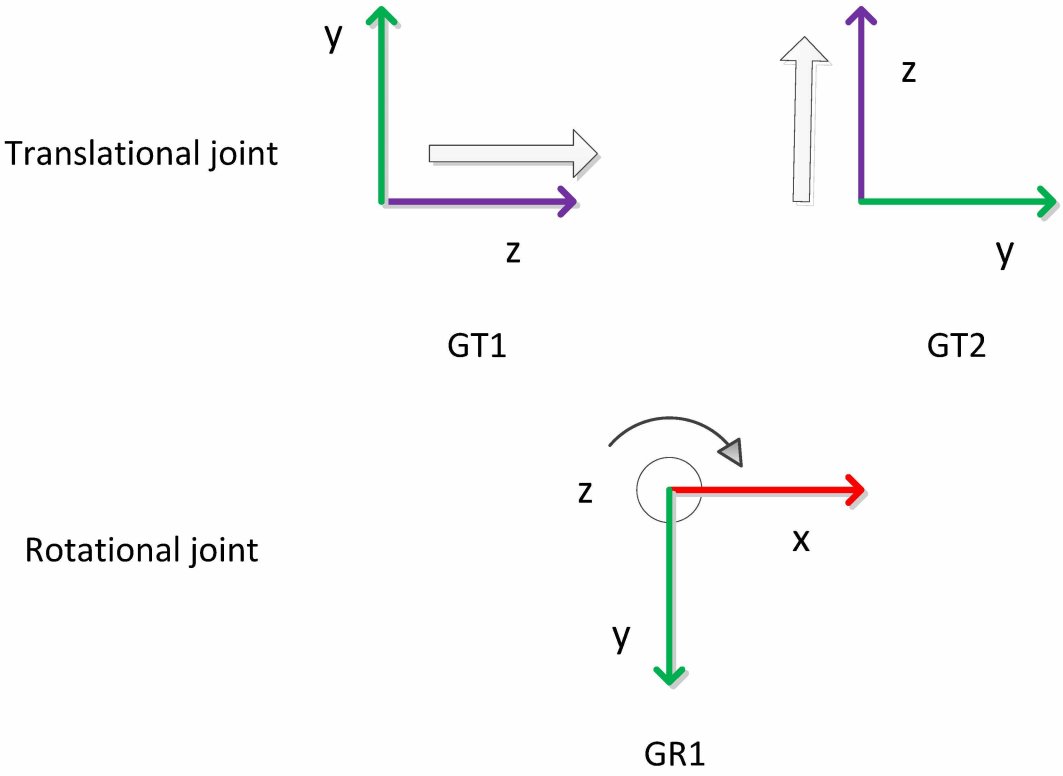

Figure 2.2 Global translation (GT) and global rotation (GR) degrees of freedom

There are three branches in the body frame. The first branch is the right leg, the second is the left leg, and the third is the spine. In the spine branch, there is an additional child branch—the arm branch including upper arm and lower arm. Each branch has a starting local frame that differs from its parent branch. Therefore, the DH table should have different values for the parent branch and its child branches.

The current digital human model has 11 degrees of freedom for the local body frame according to the DH method. The 3 global degrees of freedom bring the total to 14 degrees of freedom. A full-body digital human model is described in Figure 2.1 and Table 2.1, where θ and d represent the angle and distance along the z-axis, and a and α represent the distance and angle along the x-axis, respectively.

Table 2.1 DH table for digital human

DOF	**θ**	**d**	**a**	**α**	**Segment**
GT1	π	0	0	$\pi/2$	global translation
GT2	$\pi/2$	L_1+L_2	0	$-\pi/2$	
GR1 (to right leg)	0	0	0	0	global rotation
GR1 (to left leg)	0	0	0	0	
GR1 (to spine)	0	0	0	0	
Q1	$-\pi/2$	0	L_5	0	spine
Q2	π	0	L_6	0	arm
Q3	0	0	L_7	0	
Q4	$\pi/2$	0	L_1	0	right leg
Q5	0	0	L_2	0	
Q6	$-\pi/2$	0	L_3	0	
Q7	0	0	L_4	0	
Q8	$\pi/2$	0	L_1	0	left leg
Q9	0	0	L_2	0	

Table 2.2.1 cont.

Q10	$-\pi/2$	0	L_3	0	
Q11	0	0	L_4	0	

2.3 Anthropometric Data

The anthropometric data for the skeletal model representing a 50th percentile male are generated using GEBOD [3] software. Link length (L), mass and moment of inertia are shown in Table 2.2. Physical joint angle limits are shown in Table 2.3. Physical joint torque limits are shown in Table 2.4.

Table 2.2 Link length, mass, and moment of inertia

Link name	Link length (m)	Link mass (kg)	Moment of inertia, I_{ZZ} ($kg \cdot m^2$)
Link 1	0.383	9.54	1.014
Link 2	0.395	3.74	0.317
Link 3	0.090	0.70	0.0009
Link 4	0.100	0.23	0.0003
Link 5	0.345	9.28	0.116
Link 6	0.259	1.90	0.067
Link 7	0.247	1.34	0.041

Table 2.3 Joint angle limits (degree)

Joint name	Lower limit	Upper limit
Global translation 1 (forward)	-5.0 (m)	5.0 (m)
Global translation 2 (upward)	-5.0 (m)	5.0 (m)
Global rotation	0.0	0.0

Table 2.3 cont.

Spine	0.0	90.0
Shoulder	-180.0	90.0
Elbow	-150.0	0.0
Hip	-100.0	90.0
Knee	0.0	120.0
Ankle	-20.0	80.0
Metatarsophalangeal	-60.0	0.0

Table 2.4 Joint torque limits (N·m)

Joint name	Lower limit	Upper limit
Global translation 1 (forward)	-500.0	500.0
Global translation 2 (upward)	-500.0	500.0
Global rotation	-500.0	500.0
Spine	-500.0	500.0
Shoulder	-92.0	63.0
Elbow	-58.7	60.3
Hip	-167.0	204.0
Knee	-259.1	103.2
Ankle	-200.0	200.0
Metatarsophalangeal	-70.0	70.0

Chapter 3 Kinematics and Dynamics

The Denavit-Hartenberg [6] method is applied for the kinematics analysis. This method represents each link coordinate system in terms of the previous link coordinate system. Any local coordinate system can be expressed in global reference frame by the DH method. So, basically, the method represents a vector in one coordinate frame in terms of another coordinate frame. This method has its base in the field of robotics, but it can be used for modeling human kinematics as well.

3.1 Denavit-Hartenberg method

Consider an articulated chain depicted in Figure 3.1.

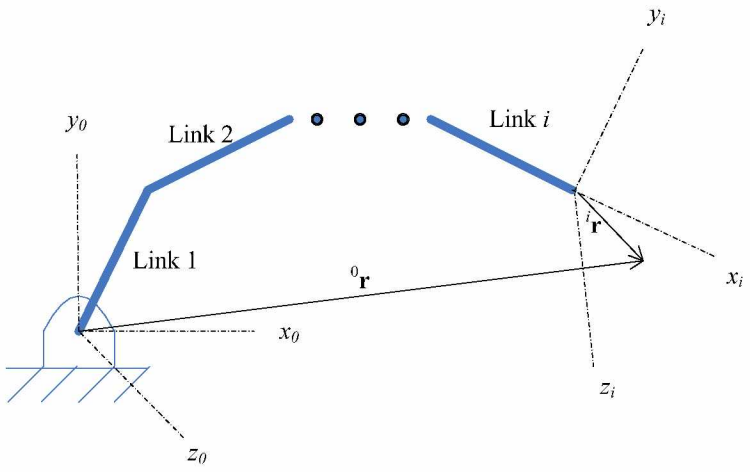

Figure 3.1 Articulated chain

Any point of interest in the i[th] frame ${}^i\mathrm{r}$ can be transferred to the global reference frame ${}^0\mathbf{r}$:

$$ {}^0\mathbf{r} = {}^0\mathbf{T}_i \, {}^i\mathbf{r} \tag{3.1} $$

where ${}^i\mathbf{r}$ is a 4×1 vector in terms of the i[th] reference frame and ${}^0\mathrm{T}_i$ is a 4×4 homogeneous transformation matrix from the i[th] reference frame to the global reference frame. The format of the vector ${}^i\mathbf{r}$ is

$$ {}^i\mathbf{r} = \begin{bmatrix} r_x & r_y & r_z & 1 \end{bmatrix}^T \tag{3.2} $$

where r_x, r_y, and r_z represent any point of interest in the i^{th} frame in terms of the Cartesian coordinates.

Here the transformation of a vector to the global reference frame is simply the multiplication of transformation matrices, which is given as:

$$ {}^{0}\mathbf{T}_i = {}^{0}\mathbf{T}_1 {}^{1}\mathbf{T}_2 \mathrm{L}\ {}^{i-1}\mathbf{T}_i = \prod_{n=1}^{i} {}^{n-1}\mathbf{T}_n \tag{3.3} $$

The transformation matrix is a 4×4 matrix that includes 4 DH parameters, which are described in Figure 3.2.

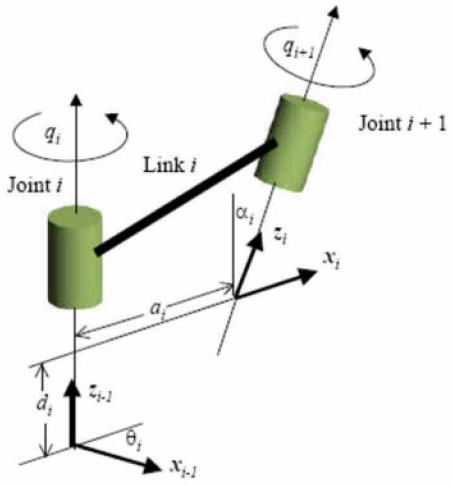

Figure 3.2 DH parameters.

According to the DH method, the four DH parameters in Figure 3.2 are defined as θ_i, d_i, a_i, and α_i, which relate coordinate frames i and i-1. Then, the transformation matrix ${}^{i-1}\mathbf{T}_i$ is composed in the following sequence of transformations:

$$ {}^{i-1}\mathbf{T}_i = \mathbf{R}_z(\theta_i)\mathbf{Trans}_z(d_i)\mathbf{Trans}_x(a_i)\mathbf{R}_x(\alpha_i) \tag{3.4} $$

where R_z and R_x represent rotation about the z and x axes, respectively, and $Trans_x$ represent translations along the z and x axes, respectively.

The DH transformation matrix from the i-1^{th} frame to the i^{th} frame is then given as:

$$ {}^{i-1}\mathbf{T}_i = \begin{bmatrix} \cos\theta_i & -\cos\alpha_i \sin\theta_i & \sin\alpha_i \sin\theta_i & a_i \cos\theta_i \\ \sin\theta_i & \cos\alpha_i \cos\theta_i & -\sin\alpha_i \cos\theta_i & a_i \sin\theta_i \\ 0 & \sin\alpha_i & \cos\alpha_i & d_i \\ 0 & 0 & 0 & 1 \end{bmatrix} \tag{3.5} $$

In the case of a rotational joint, the joint parameters d_i, a_i, and α_i are constant (which means they are fixed). Only θ_i is treated as a rotational degree of freedom, q_i. In a mechanical model, q_i is the vector of generalized coordinates, and each transformation matrix has one degree of freedom.

3.2 Forward Recursive Kinematics

The kinematics analysis in the recursive form leads to a simpler form for the transformation matrix A_i. The time derivatives of the transformation matrix $\mathbf{A}_i$ can be obtained in the recursive form as well:

$$ \mathbf{A}_i = \mathbf{A}_{i-1}\, {}^{i-1}\mathbf{T}_i \tag{3.6} $$

$$ \mathbf{B}_j = \dot{\mathbf{A}}_j = \mathbf{B}_{j-1}\mathbf{T}_j + \mathbf{A}_{j-1}\frac{\partial \mathbf{T}_j}{\partial q_j}\dot{q}_j \tag{3.7} $$

$$ \begin{aligned} \mathbf{C}_j = \dot{\mathbf{B}}_j = \ddot{\mathbf{A}}_j &= \mathbf{C}_{j-1}\mathbf{T}_j + 2\mathbf{B}_{j-1}\frac{\partial \mathbf{T}_j}{\partial q_j}\dot{q}_j \\ &+ \mathbf{A}_{j-1}\frac{\partial^2 \mathbf{T}_j}{\partial q_j^2}\dot{q}_j^2 + \mathbf{A}_{j-1}\frac{\partial \mathbf{T}_j}{\partial q_j}\ddot{q}_j \end{aligned} \tag{3.8} $$

where q_i is the joint angle, ${}^{i-1}\mathbf{T}_i$ is the link transformation matrix, and $\mathbf{A}_0 = [\mathbf{I}]$, $\mathbf{B}_0 = \mathbf{C}_0 = [\mathbf{0}]$. The derivatives of the transformation matrices with respect to joint angles, joint angle velocities, and joint angle accelerations are

$$ \frac{\partial \mathbf{A}_i}{\partial q_k} = \begin{cases} \mathbf{A}_{i-1}\dfrac{\partial\, {}^{i-1}\mathbf{T}_i}{\partial q_k} & (k = i) \\ \dfrac{\partial \mathbf{A}_{i-1}}{\partial q_k}\, {}^{i-1}\mathbf{T}_i & (k < i) \end{cases} \tag{3.9} $$

$$\frac{\partial \mathbf{B}_i}{\partial q_k} = \begin{cases} \frac{\partial \mathbf{B}_{i-1}}{\partial q_k}\mathbf{T}_i + \frac{\partial \mathbf{A}_{i-1}}{\partial q_k}\frac{\partial \mathbf{T}_i}{\partial q_i}\dot{q}_i & (k < i) \\ \mathbf{B}_{i-1}\frac{\partial \mathbf{T}_i}{\partial q_k} + \mathbf{A}_{i-1}\frac{\partial^2 \mathbf{T}_i}{\partial q_k^2}\dot{q}_i & (k = i) \\ \mathbf{0} & (k > i) \end{cases} \tag{3.10}$$

$$\frac{\partial \mathbf{B}_i}{\partial \dot{q}_k} = \begin{cases} \frac{\partial \mathbf{B}_{i-1}}{\partial \dot{q}_k}\mathbf{T}_i & (k < i) \\ \mathbf{A}_{i-1}\frac{\partial \mathbf{T}_i}{\partial q_k} & (k = i) \\ \mathbf{0} & (k > i) \end{cases} \tag{3.11}$$

$$\frac{\partial \mathbf{C}_i}{\partial q_k} = \begin{cases} \frac{\partial \mathbf{C}_{i-1}}{\partial q_k}\mathbf{T}_i + 2\frac{\partial \mathbf{B}_{i-1}}{\partial q_k}\frac{\partial \mathbf{T}_i}{\partial q_i}\dot{q}_i + \frac{\partial \mathbf{A}_{i-1}}{\partial q_k}\frac{\partial^2 \mathbf{T}_i}{\partial q_i^2}\dot{q}_i^2 \\ \qquad + \frac{\partial \mathbf{A}_{i-1}}{\partial q_k}\frac{\partial \mathbf{T}_i}{\partial q_i}\ddot{q}_i \\ \mathbf{C}_{i-1}\frac{\partial \mathbf{T}_i}{\partial q_k} + 2\mathbf{B}_{i-1}\frac{\partial^2 \mathbf{T}_i}{\partial q_k^2}\dot{q}_i + \mathbf{A}_{i-1}\frac{\partial^3 \mathbf{T}_i}{\partial q_k^3}\dot{q}_i^2 \\ \qquad + \mathbf{A}_{i-1}\frac{\partial^2 \mathbf{T}_i}{\partial q_k^2}\ddot{q}_i \\ \mathbf{0} \end{cases} \tag{3.12}$$

$$\frac{\partial \mathbf{C}_i}{\partial \dot{q}_k} = \begin{cases} \frac{\partial \mathbf{C}_{i-1}}{\partial \dot{q}_k}\mathbf{T}_i + 2\frac{\partial \mathbf{B}_{i-1}}{\partial \dot{q}_k}\frac{\partial \mathbf{T}_i}{\partial q_i}\dot{q}_i & (k < i) \\ 2\mathbf{B}_{i-1}\frac{\partial \mathbf{T}_i}{\partial q_k} + 2\mathbf{A}_{i-1}\frac{\partial^2 \mathbf{T}_i}{\partial q_k^2}\dot{q}_i & (k = i) \\ \mathbf{0} & (k > i) \end{cases} \tag{3.13}$$

$$\frac{\partial \mathbf{C}_i}{\partial \ddot{q}_k} = \begin{cases} \frac{\partial \mathbf{C}_{i-1}}{\partial \ddot{q}_k}\mathbf{T}_i & (k < i) \\ \mathbf{A}_{i-1}\frac{\partial \mathbf{T}_i}{\partial q_k} & (k = i) \\ \mathbf{0} & (k > i) \end{cases} \tag{3.14}$$

3.3 Backward Recursive Dynamics

Based on forward recursive kinematics, the backward recursion for the dynamic analysis is accomplished by defining a 4×4 transformation matrix $\mathbf{D}_i$ and 4×1 transformation vectors $\mathbf{E}_i$, $\mathbf{F}_i$, and $\mathbf{G}_i$ as follows: given the mass and inertia properties of each link, the external force $\mathbf{f}_k^{\mathrm{T}} = \begin{bmatrix} {}^k f_x & {}^k f_y & {}^k f_z & 0 \end{bmatrix}$ and the moment $\mathbf{h}_k^{\mathrm{T}} = \begin{bmatrix} {}^k h_x & {}^k h_y & {}^k h_z & 0 \end{bmatrix}$ for the link k, defined in the global coordinate system, the joint actuation torques τ_i for i = n to 1 are computed as:

$$\tau_i = tr[\ \frac{\partial \mathbf{A}_i}{\partial q_i}\mathbf{D}_i] - \mathbf{g}^{\mathrm{T}}\frac{\partial \mathbf{A}_i}{\partial q_i}\mathbf{E}_i - \mathbf{f}_k^{\mathrm{T}}\frac{\partial \mathbf{A}_i}{\partial q_i}\mathbf{F}_i - \mathbf{G}_i^{\mathrm{T}}\mathbf{A}_{i-1}\mathbf{z}_0 \tag{3.15}$$

$$\mathbf{D}_i = \mathbf{J}_i\mathbf{C}_i^{\mathrm{T}} + \mathbf{T}_{i+1}\mathbf{D}_{i+1} \tag{3.16}$$

$$\mathbf{E}_i = m_i\,{}^i\mathbf{r}_i + \mathbf{T}_{i+1}\mathbf{E}_{i+1} \tag{3.17}$$

$$\mathbf{F}_i = {}^k\mathbf{r}_f\delta_{ik} + \mathbf{T}_{i+1}\mathbf{F}_{i+1} \tag{3.18}$$

$$\mathbf{G}_i = \mathbf{h}_k\delta_{ik} + \mathbf{G}_{i+1} \tag{3.19}$$

where $\mathbf{D}_{n+1} = \mathbf{0}$ and $\mathbf{E}_{n+1} = \mathbf{F}_{n+1} = \mathbf{G}_{n+1} = \mathbf{0}$; $\mathbf{J}_i$ is the inertia matrix for link i; m_i is the mass of link i; $\mathbf{g}$ is the gravity vector; ${}^i\mathbf{r}_i$ is the location of center of mass of link i in the local frame i; ${}^k\mathbf{r}_f$ is the position of the external force in the local frame k; $\mathbf{z}_0 = \begin{bmatrix} 0 & 0 & 1 & 0 \end{bmatrix}^{\mathrm{T}}$ for a revolute joint and $\mathbf{z}_0 = \begin{bmatrix} 0 & 0 & 0 & 0 \end{bmatrix}^{\mathrm{T}}$ for a prismatic joint; and, finally, δ_{ik} is Kronecker delta.

The first term in the torque expression (equation of motion) is the inertia and Coriolis torque, the second term is the torque due to gravity load, the third term is the torque due to external force, and the fourth term represents the torque due to the external moment.

The derivatives, $\frac{\partial \tau_i}{\partial q_k}$, $\frac{\partial \tau_i}{\partial \dot{q}_k}$, $\frac{\partial \tau_i}{\partial \ddot{q}_k}$ (i = 1 to n; k = 1 to n), can be evaluated for the articulated spatial human mechanical system in a recursive way using the foregoing recursive Lagrangian dynamics formulation as follows:

$$\frac{\partial \tau_i}{\partial q_k} = \begin{cases} tr\left(\frac{\partial^2 \mathbf{A}_i}{\partial q_i \partial q_k}\mathbf{D}_i + \frac{\partial \mathbf{A}_i}{\partial q_i}\frac{\partial \mathbf{D}_i}{\partial q_k}\right) - \mathbf{g}^{\mathrm{T}}\frac{\partial^2 \mathbf{A}_i}{\partial q_i \partial q_k}\mathbf{E}_i - \mathbf{f}^{\mathrm{T}}\frac{\partial^2 \mathbf{A}_i}{\partial q_i \partial q_k}\mathbf{F}_i - \mathbf{G}_i{}^{\mathrm{T}}\frac{\partial \mathbf{A}_{i-1}}{\partial q_k}\mathbf{z}_0 & (k \le i) \\ tr\left(\frac{\partial \mathbf{A}_i}{\partial q_i}\frac{\partial \mathbf{D}_i}{\partial q_k}\right) - \mathbf{g}^{\mathrm{T}}\frac{\partial \mathbf{A}_i}{\partial q_i}\frac{\partial \mathbf{E}_i}{\partial q_k} - \mathbf{f}^{\mathrm{T}}\frac{\partial \mathbf{A}_i}{\partial q_i}\frac{\partial \mathbf{F}_i}{\partial q_k} & (k > i) \end{cases} \tag{3.20}$$

$$\frac{\partial \tau_i}{\partial \dot{q}_k} = tr\left(\frac{\partial \mathbf{A}_i}{\partial q_i}\frac{\partial \mathbf{D}_i}{\partial \dot{q}_k}\right) \tag{3.21}$$

$$\frac{\partial \tau_i}{\partial \ddot{q}_k} = tr\left(\frac{\partial \mathbf{A}_i}{\partial q_i}\frac{\partial \mathbf{D}_i}{\partial \ddot{q}_k}\right) \tag{3.22}$$

Chapter 4 Lifting Simulation

In this chapter, lifting motion is studied. The problem is formulated as a nonlinear optimization problem. The program SNOPT [10], based on a sequential quadratic programming (SQP) approach, is used to solve the optimization problem. Different weight of the box is considered for the simulation and cause and effect is studied. In addition to the kinematics data, kinetics data such as joint torques and ground reaction forces are recovered from the simulation.

In this work, the lifting task is defined as moving a box from an initial location to a final location in vertical plane. Figure 4.1 depicts the input parameters for the proposed formulation. In this regard, h_1 is the initial height of the box measured from the ground, d_1 is the initial distance measured from the foot location to the center of the box; h_2 is the final height measured from the ground, d_2 is the final distance, and w is the weight of the box. The initial and final postures and dynamic lifting trajectory are solved from a nonlinear optimization problem. In addition, the mechanical system is at rest at the initial and final times.

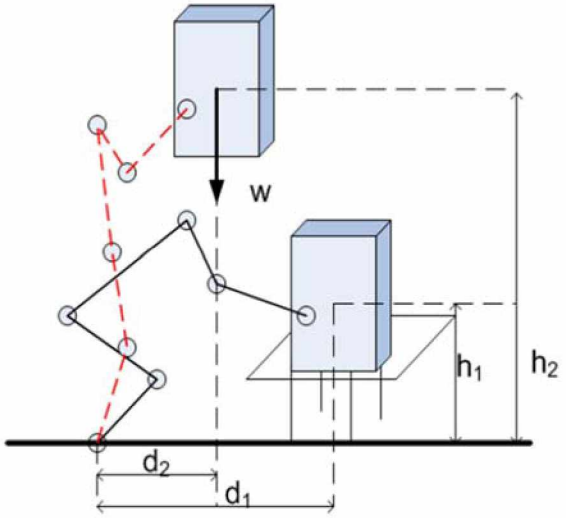

Figure 4.1 Input parameters for the lifting task

4.1 Optimization Formulation

For the task of lifting an object, given values consist of: initial and final location of object, feet location and orientation, and box weight. The duration of lifting time T is an input specified variable. The

motion of lifting is predicted via solving an optimization problem. The initial and final postures as well as lifting motion are also determined by optimization instead of using experimental data.

Design Variables

The only design variable are the joint angles: $\mathbf{q(t)}$. The joint-torques are then calculated from an inverse dynamics procedure based on current joint profiles. No integration is done on the governing differential equations. The joint angle profiles are discretized using cubic B-splines. Therefore, the continuous optimal control problem is transferred into a nonlinear programming (NLP) optimization problem. Each DOF is represented by 4 B-spline control points, and the total design variables are $4 \times 14 = 56$.

Objective Function

The goal is to determine the optimal motion to minimize the dynamic effort required to lift the box. Therefore, the force is determined by the time integral of the square of all joint toques:

$$F(q) = \sum_{i=3}^{n} \int_{t=0}^{T} \left(\frac{\tau_i(q)}{\tau_i(q)^U - \tau_i(q)^L} \right)^2 dt \qquad (4.1)$$

where n is the number of degrees of freedom, T is the total time, τ_i^U is the upper torque limit for ith joint and τ_i^L lower limit. The total time duration T is a specified input parameter.

Constraints

There are two forms of constrains that need to be accounted for: time-dependent and time-independent. Time-dependent constraints include: (1) joint angle limits, (2) torque limits, (3) foot contacting position, (4) dynamic stability, and (5) body collision avoidance. These constraints are accounted for throughout the time interval, T. Time-independent constraints include (6) initial and final box locations, and (7) static conditions at the beginning and end of the motion. From time discretization, it is determined that there are 223 total nonlinear constraints. Finally, the formulated NPL is solved using the optimization

software SNOPT [10].

4.2 Results

The flowchart below illustrates the programing procedure:

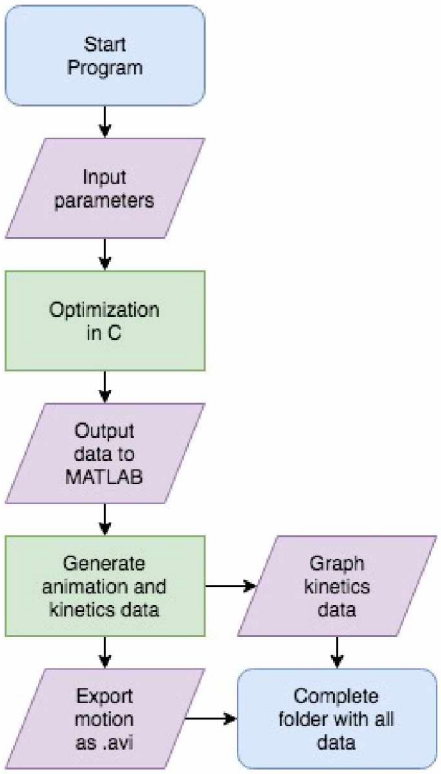

Varying weight

In this simulation, the foot locations and time duration are specified for a lifting task. Given the box initial location (d_1 = 0.5 m, h_1 = 0.3 m), final location (d_2 = 0.2 m, h_2 = 1.0 m), and weight (w = 80 N), the dynamic lifting motion is predicted to minimize the performance measure, dynamic effort, and subject to physical constraints. The total time is 1 second. Figure 4.2 shows the resulting optimal lifting motion. As expected, correct bending of the knee and spine occur to generate the optimal lifting motion. This is a typical back lift, which is successfully predicted by the current formulation. The joint angle profiles are depicted in Figure 4.3.

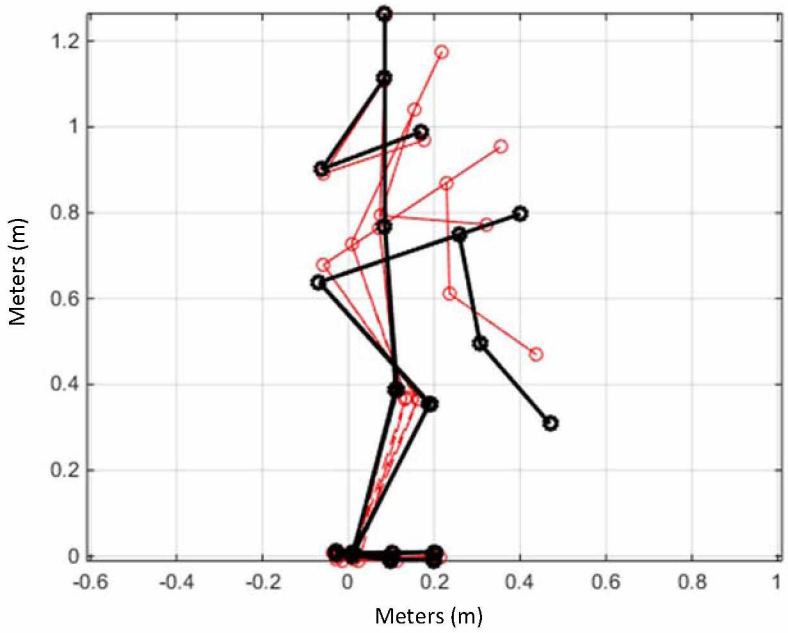

Figure 4.2 Optimal lifting motions for 80 N lift at 1.0 s duration

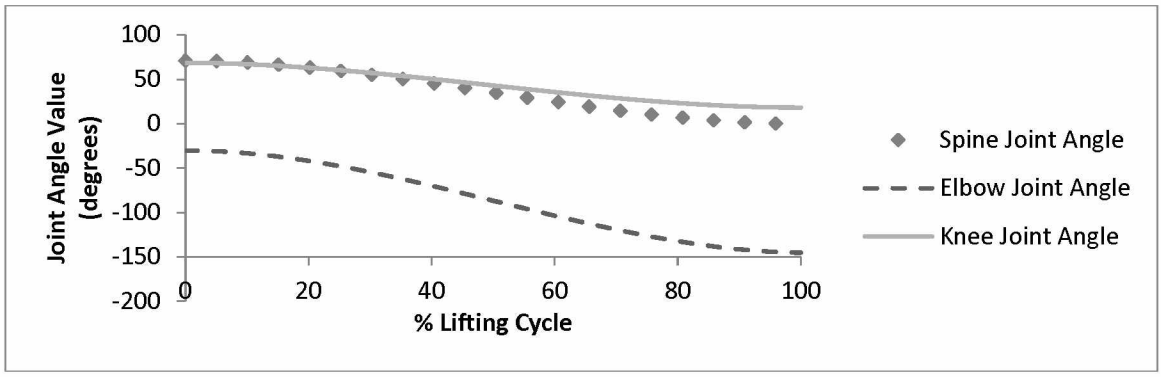

Figure 4.3 Optimal joint angles for 80 N lift at 1.0 s duration

To study cause-and-effect, a variance in weight of the box is used in varying simulations. The same lifting task is optimized with the box weight decreased to 40 N and the optimal lifting motion of the simulation is obtained as shown in Figure 4.4. In addition, GRF and joint torque profiles obtained from the motion prediction are shown in Figures 4.5, 4.6, 4.7, 4.8, and 4.9, respectively.

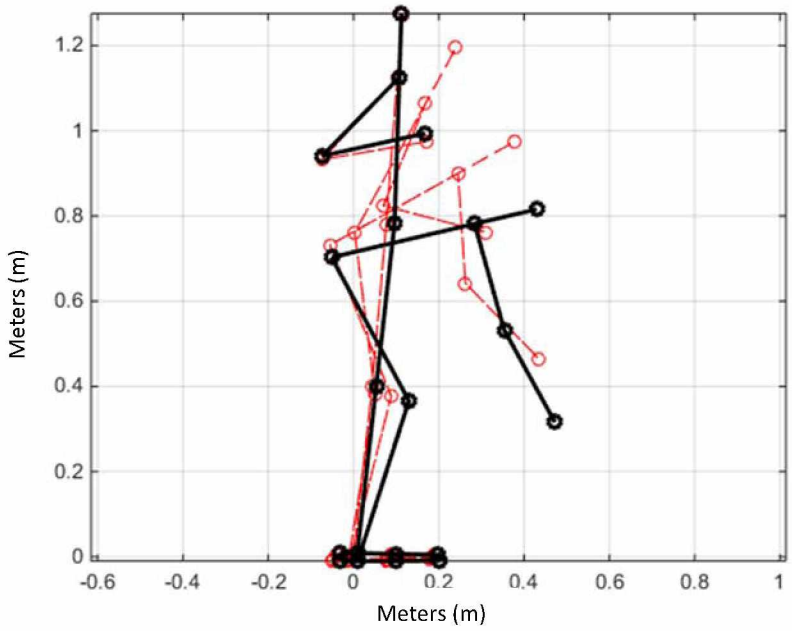

Figure 4.4 Optimal lifting motions for 40 N lift at 1.0 s duration

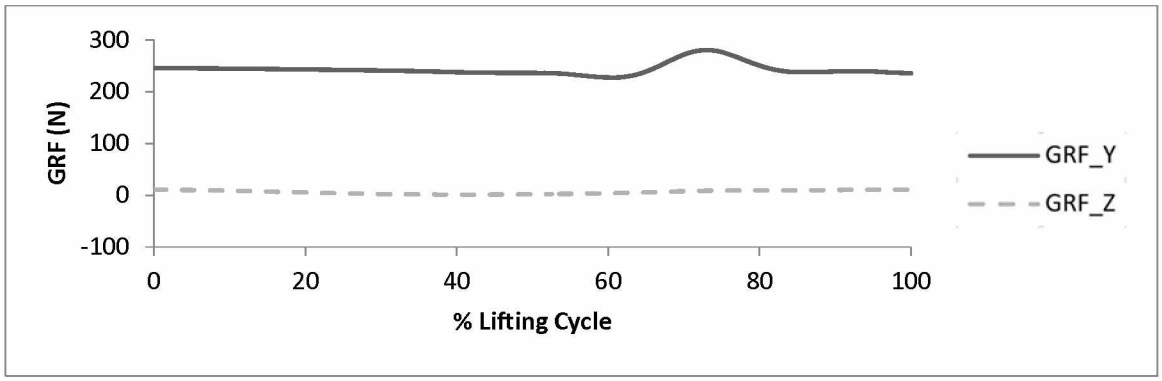

Figure 4.5 Ground reactive forces for 80 N lift at 1.0 s duration

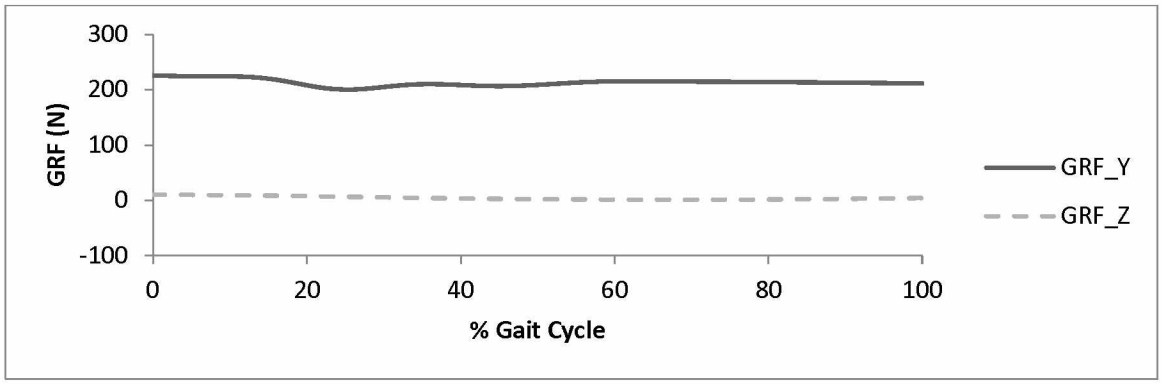

Figure 4.6 Ground reactive forces for 40 N lift at 1.0 s duration

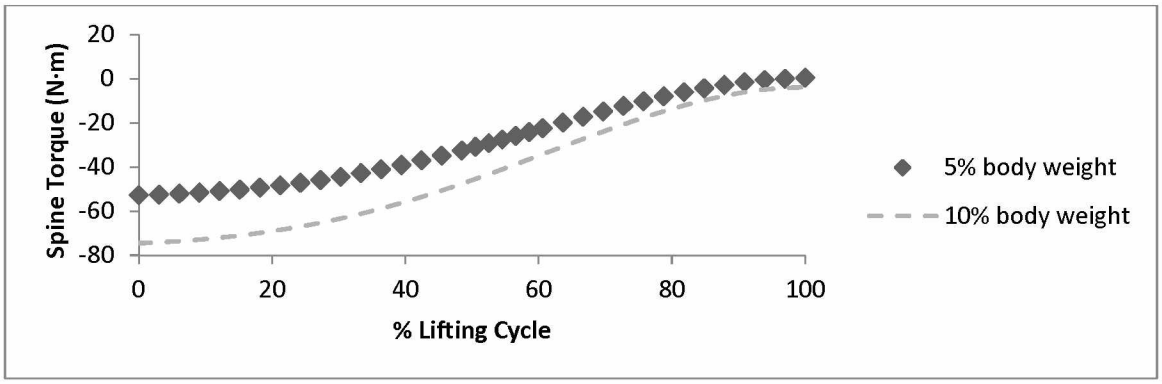

Figure 4.7 Spine joint torques over two weights

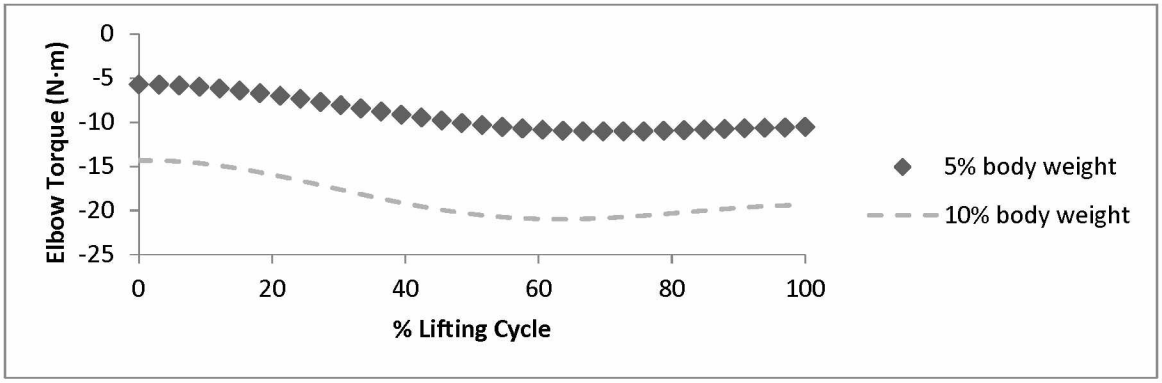

Figure 4.8 Elbow joint torques over two weights

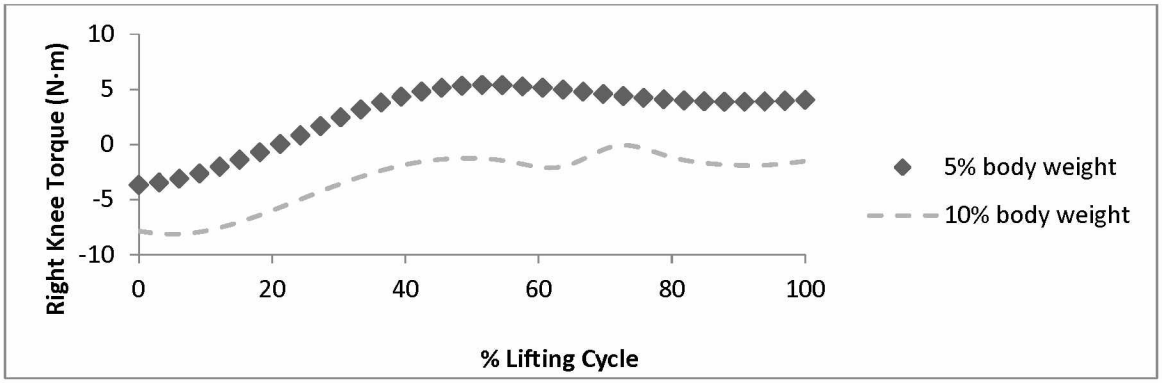

Figure 4.9 Right knee joint torques over two weights

Varying speed

To further study cause-and-effect, varied lifting time is used in the simulation. The same lifting task with the box weight 80 N is optimized while the lifting time is reduced to 0.6 s and then increased to 1.4 s, and the respective optimal lifting motions are obtained in Figure 4.10 and Figure 4.11. The GRF and joint torque profiles obtained from the motion prediction are shown in Figures 4.12 and 4.13, 4.14, 4.15,

and 4.16, respectively.

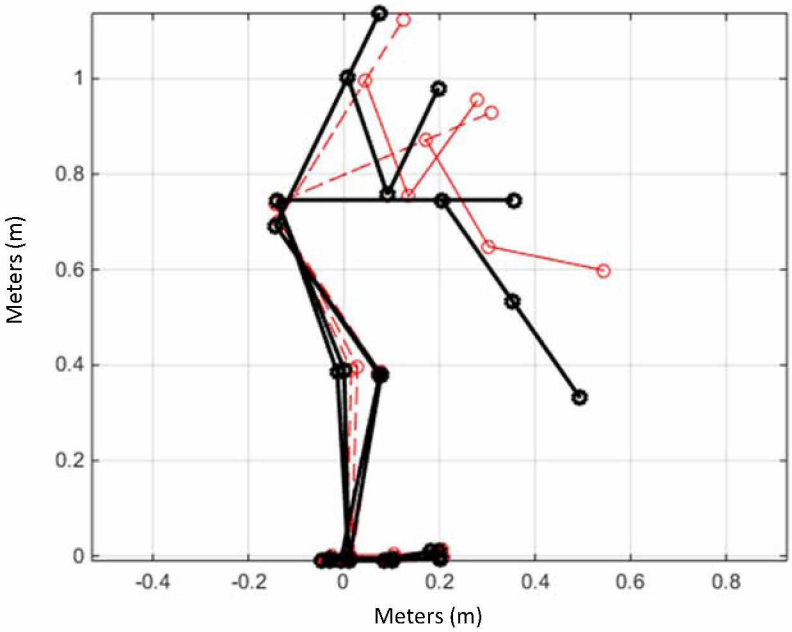

Figure 4.10 Optimal lifting motions for 80 N lift at 0.6 s duration

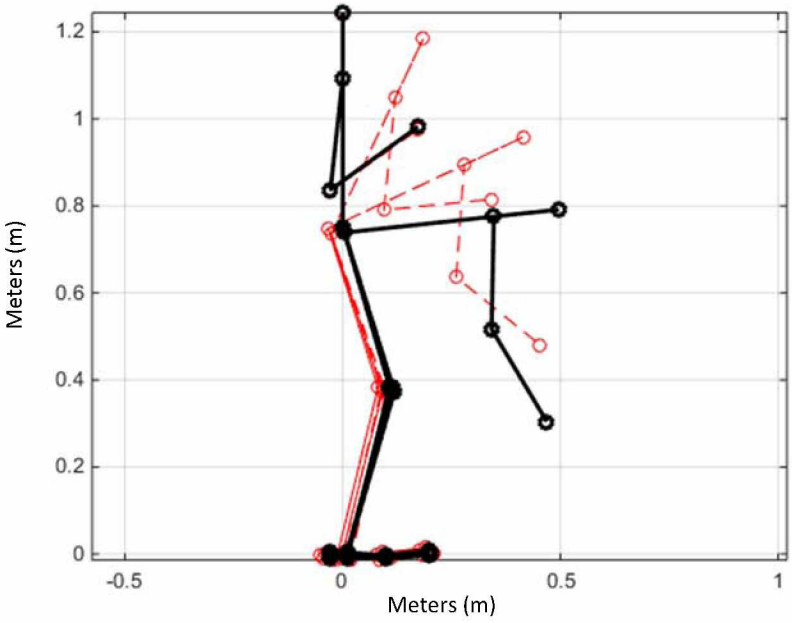

Figure 4.11 Optimal lifting motions for 80 N lift at 1.4 s duration

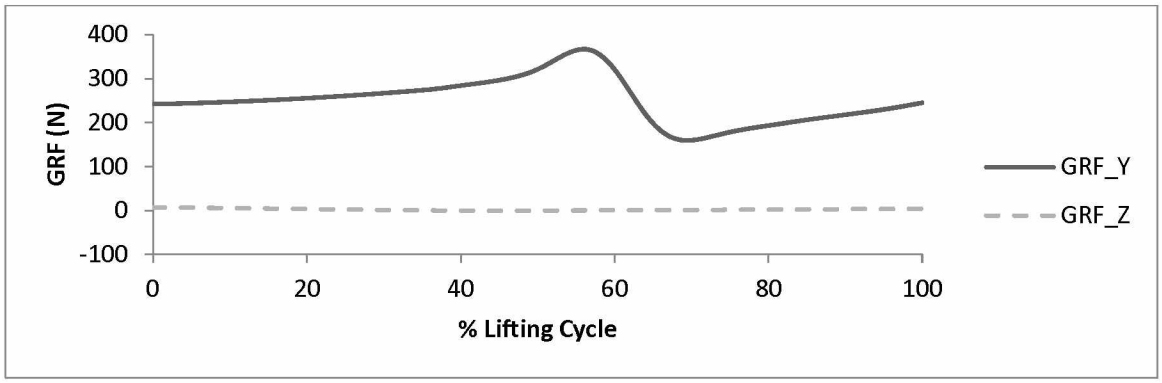

Figure 4.12 Ground reactive forces for 80 N lift at 0.6 s duration

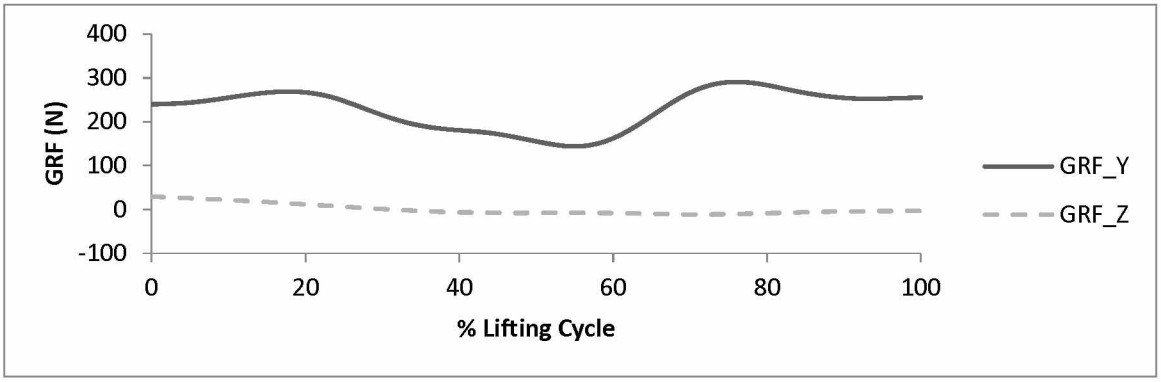

Figure 4.13 Ground reactive forces for 80 N lift at 1.4 s duration

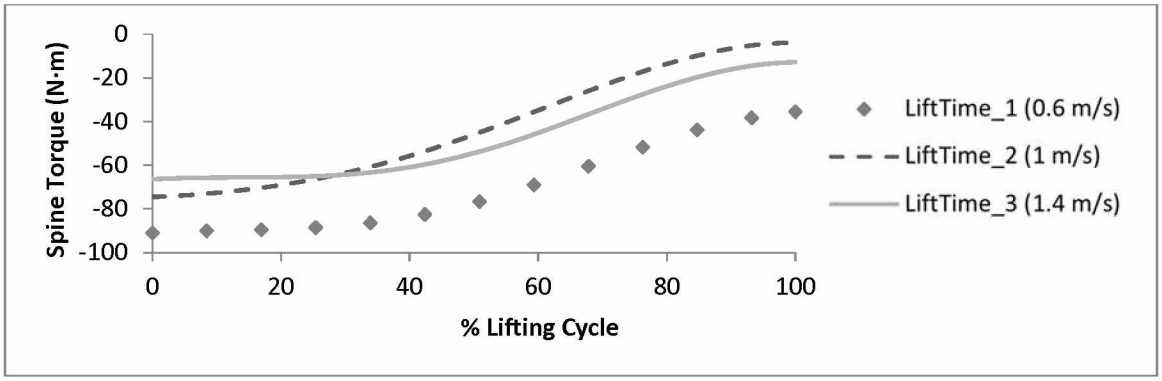

Figure 4.14 Spine joint torque over three different speeds

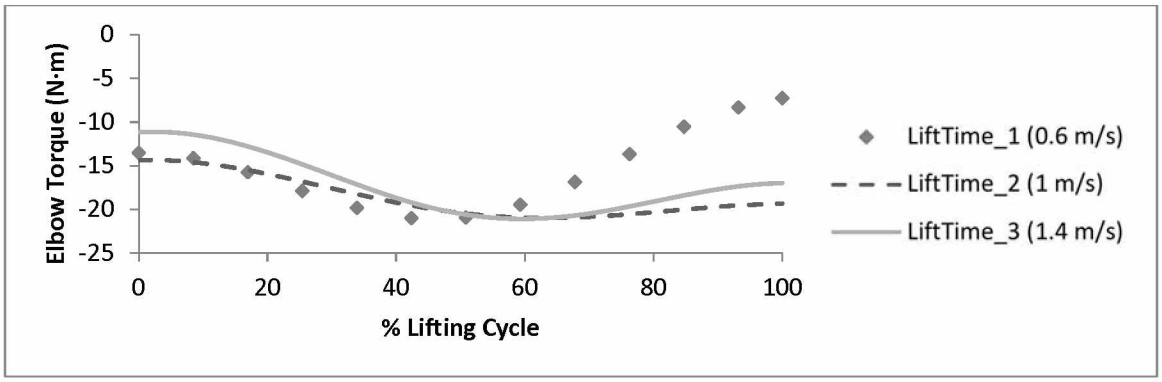

Figure 4.15 Elbow joint torques over three different speeds

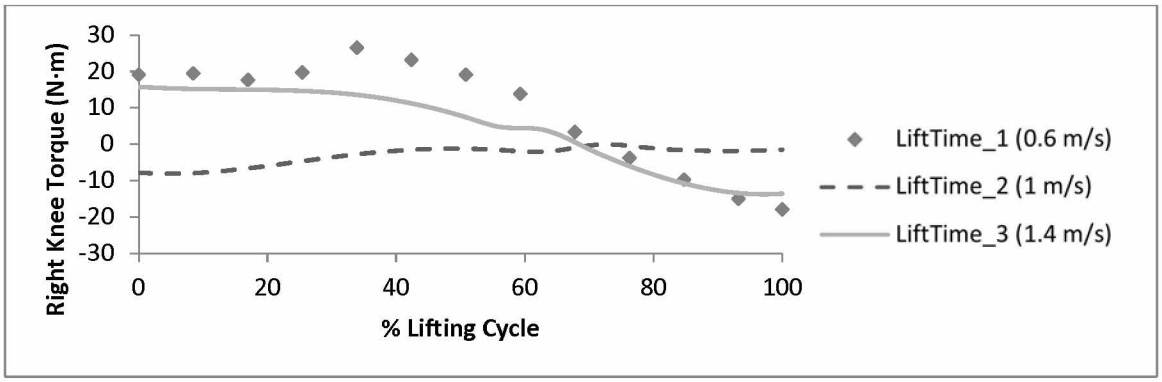

Figure 4.16 Right knee joint torques over three different speeds

Varying position

To further study cause-and-effect, a second lifting case was devised. The same lifting task with the box weight of 80 N and lift time at 1.0 s is analyzed, however both the initial and finial position of the box are changed. In case two, the starting position of the box was 0.1 m closer to the person ($d_1 = 0.4$ m), and the final position was 0.1 m higher than the original ($h_2 = 1.1$ m). The respective optimal lifting motion is obtained in Figure 4.17. The GRF and joint torque profiles for both cases are obtained from the motion prediction and shown in Figures 4.18 and 4.19, 4.20, 4.21, and 4.22, respectively.

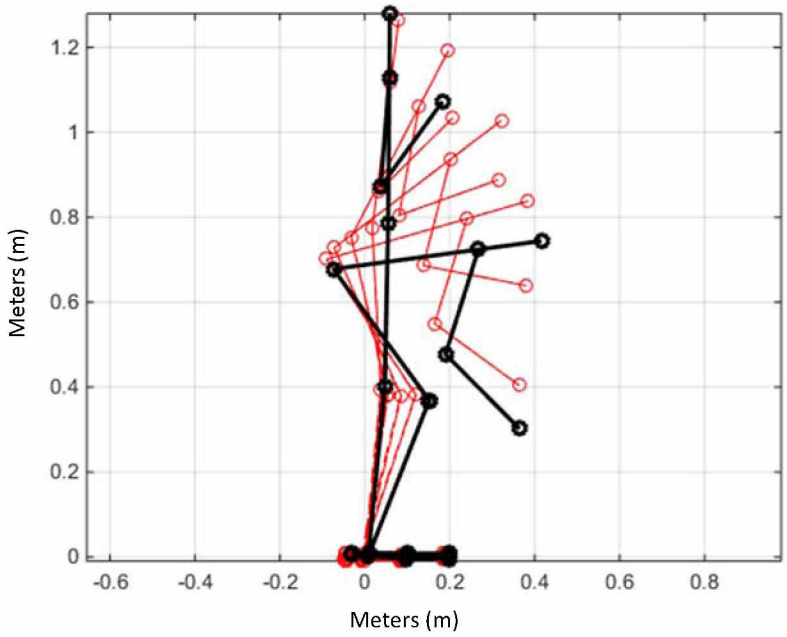

Figure 4.17 Optimal lifting motion for secondary position care (case 2)

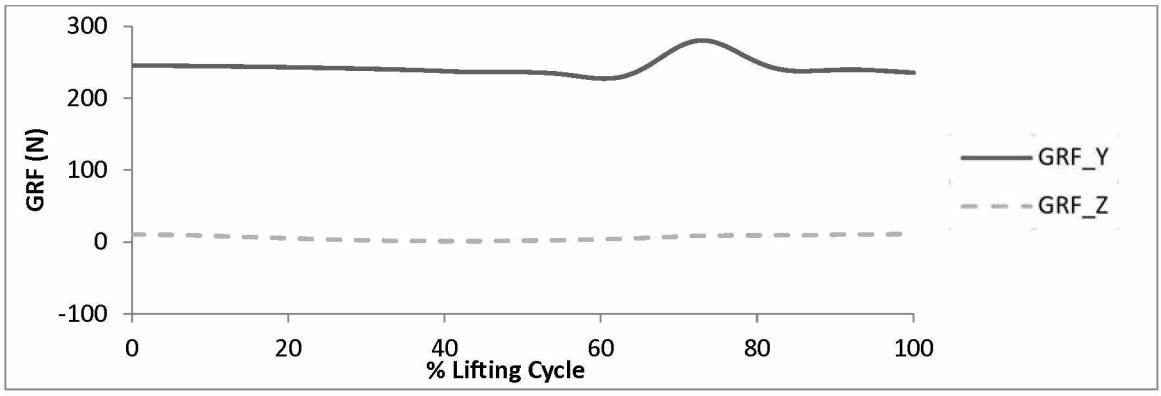

Figure 4.18 GRF for case 1

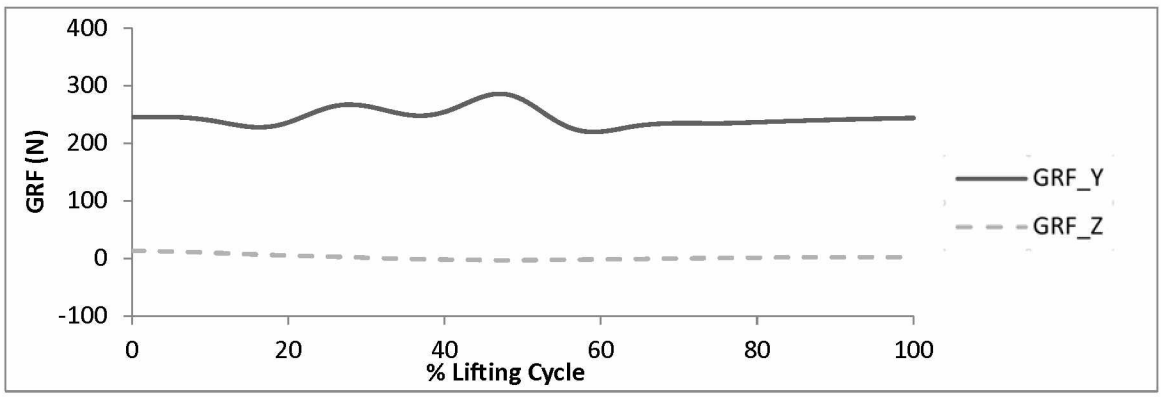

Figure 4.19 GRF for case 2

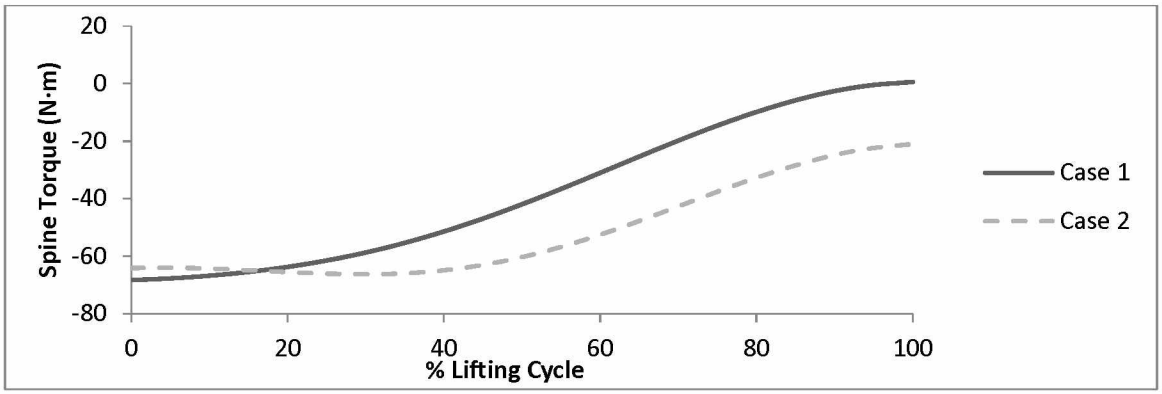

Figure 4.20 Spine joint torques over two varied positions

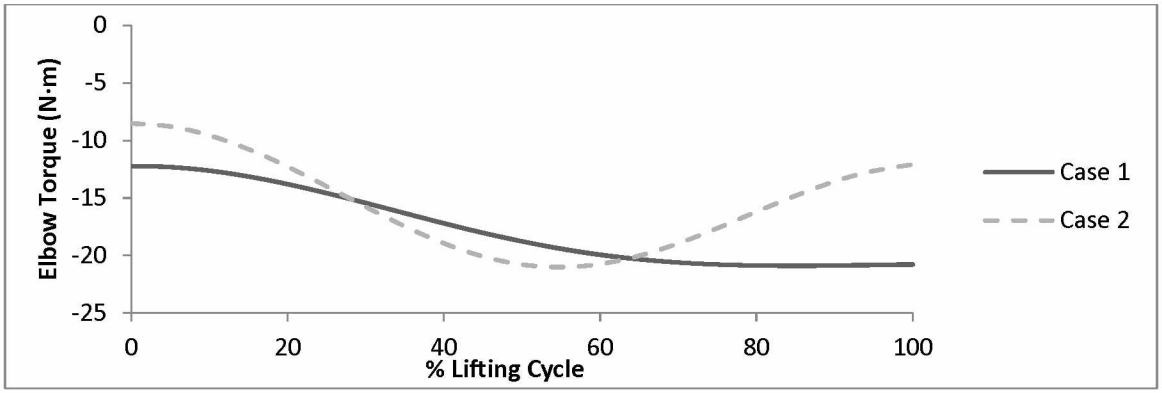

Figure 4.21 Elbow joint torques over two varied positions

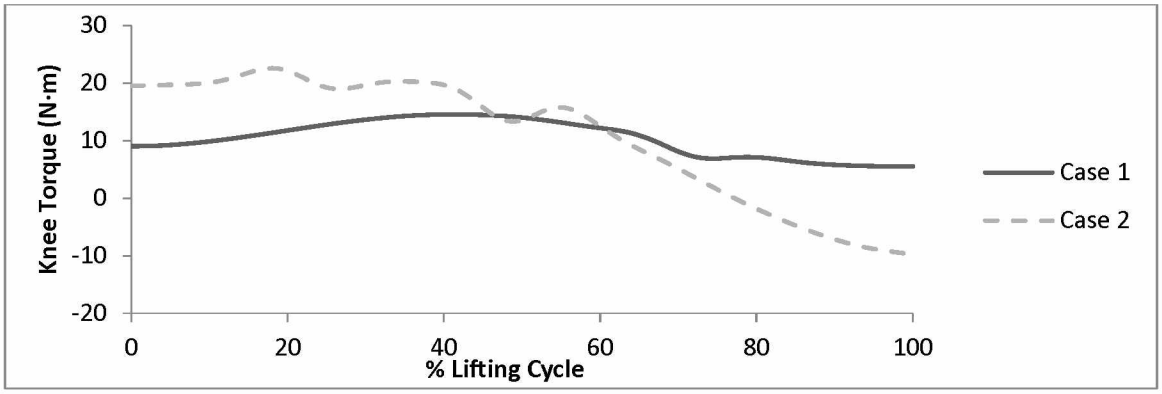

Figure 4.22 Right knee joint torques over two varied positions

4.3 Discussion

Comparing the Figures 4.3 and 4.7-4.9 to that of the published work of Xiang et al. [19, 21] it is found that the joint angle and torque profiles on the elbow, spine, and knee joints have similar trends to the published data. These similar trends affirm the validity of the simulations qualitatively.

Since the motion is just of lifting, the feet stay planted on the ground, so the GRF graphs are relatively level as seen in Figures 4.5 and 4.6. As the lifting time is decreased to 0.6 s (faster lifting), it is evident in the GRF figure that the graph shows an attempt to accelerate the box at the mid of the lifting process (Figure 4.12). Analyzing the GRF graphs, it is evident that varying the speed has a larger impact on GRF compared to varying box locations. This may be in part due to the difficultly of speeding or slowing oneself down while doing tasks. It is interesting that the fast lifting strategy is very different from normal and slow speed liftings. However, the latter two have similar lifting strategies.

For joint torques, the spine and elbow joints follow a similar trend as the input parameters are varied, however the knee torques show much greater variance between lifting runs (Figure 4.22). This interaction is also evident in the motion diagrams Figures 4.2 and 4.17, where the knees are moving differently between simulations, whereas the upper torso follows a more similar route. These results totally depend on the box locations, which means our motion prediction program can generate different lifting strategy based on input parameters for the task. In Figures 4.7, 4.8, and 4.9 we can see that heavy box results in larger joint torques. In contrast, fast lifting also has larger joint torques as shown in Figures 4.14, 4.15, and 4.16. These results are quite reasonable.

Chapter 5 Carrying Simulation

In this study, only one step carrying motion is simulated. The next step carrying motion is obtained by swapping the left and right legs motion, and the upper limb motion repeating on itself. The weight of the box is applied on hand vertically downward as a point load.

5.1 Optimization Formulation

For the task of carrying an object, given values consist of: walking speed, step lengths, and the box weight. The variables of height between box and pelvis, and horizontal distance between pelvis and box, are both determined during the optimization process along with the motion.

Design Variables

The design variable are the joint angles, $\mathbf{q}(\mathbf{t})$, and the box relative position to pelvis (h, d). Cubic B-spline functions are further used to discretize the joint angle profiles. The subsequent general equations of motion are then calculated from an inverse dynamics procedure based on current joint profiles. No integration is done on the governing differential equations.

Objective Function

The objective function is the normalized dynamic effort formulated as:

$$F(q) = \sum_{i=3}^{n} \int_{t=0}^{T} \left(\frac{\tau_i(q)}{\tau_i(q)^U - \tau_i(q)^L} \right)^2 dt \qquad (5.1)$$

where n is the number of degrees of freedom, T is the total time, τ_i^U is the upper torque limit for ith joint and τ_i^L lower limit. For the carrying process there were total 86 design variables to be optimized using SNOPT [10].

Constraints

The constraints for the carrying include: (1) joint angle limits, (2) torque limits, (3) foot contacting

position, (4) dynamic stability, (5) body collision avoidance, (6) lower body symmetric conditions and upper body continuity conditions, and (8) ground clearance. Based on B-spline discretization, it is determined that there are 783 total nonlinear constraints for carrying motion optimization.

5.2 Results

In this simulation, the walking speed and step length are specified for a carrying task. Given the box weight, the dynamic carrying motion is predicted to minimize the performance measure, dynamic effort, and subject to physical constraints. Figure 5.1 shows the resulting two-step optimal carrying motion. The joint angle profiles are depicted in Figure 5.2.

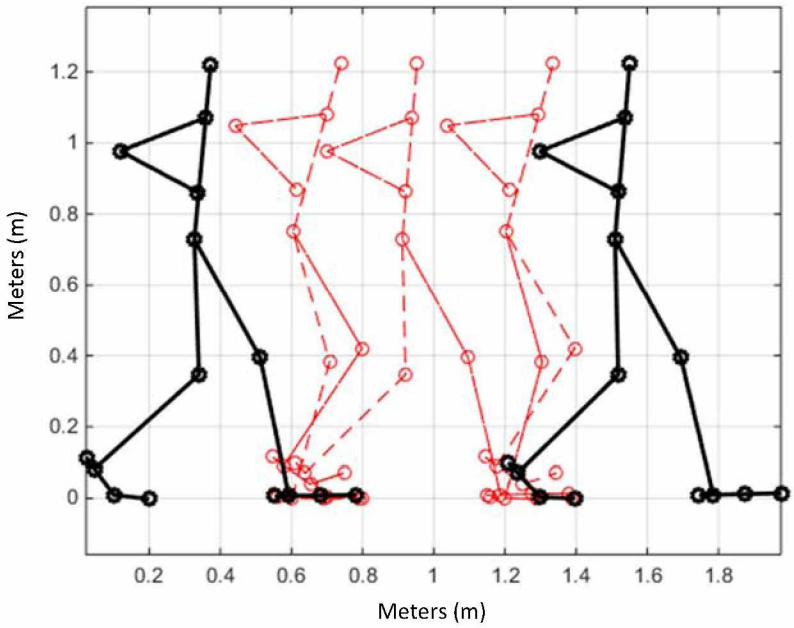

Figure 5.1 Optimal carrying motion for 80 N carry at 1.2 m/s

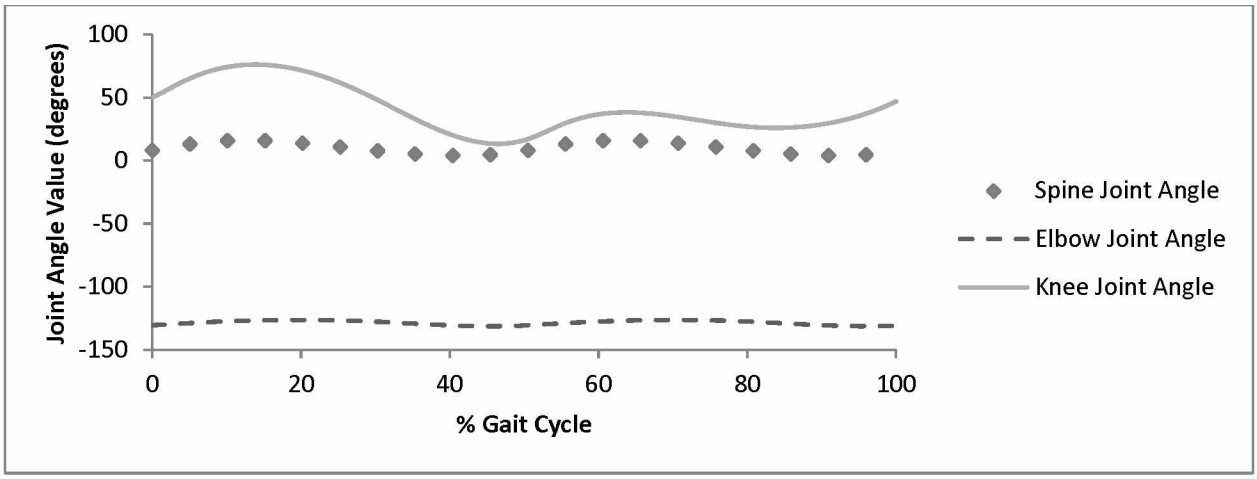

Figure 5.2 Joint angles for 80 N carry at 1.2 m/s

To study cause-and-effect, different weight of the box is used in the simulation. The same carrying task is optimized with the increased box weight (160 N), and the optimal carrying motion is obtained as shown in Figure 5.3. In addition, GRF and joint torque profiles obtained from the motion prediction are shown in Figures 5.4 through 5.8, respectively. Figure 5.4 depicts the variance in the GRF throughout the gait cycle when the weight is held at 80 N. Figure 5.5 shows the variance in the GRF when the weight is increased to 160 N. Note that GRF_Z represents the ground reactive forces in the vertical direction, and GRF_Y the forces in the forward direction.

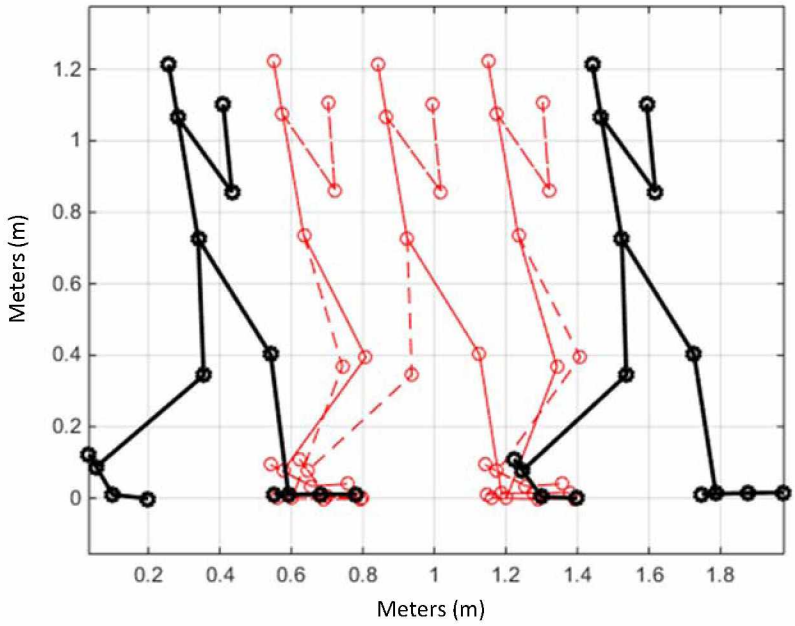

Figure 5.3 Optimal carrying motion for 160 N carry at 1.2 m/s

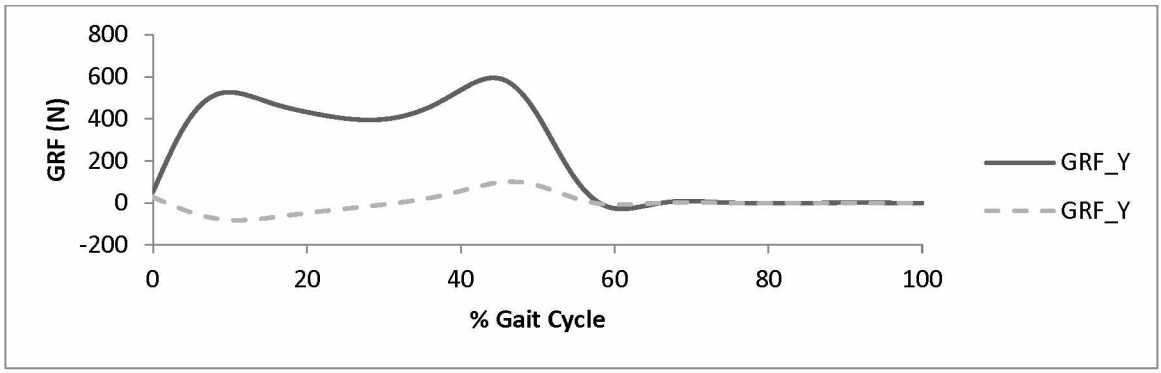

Figure 5.4 Ground reactive forces for 80 N carry at 1.2 m/s

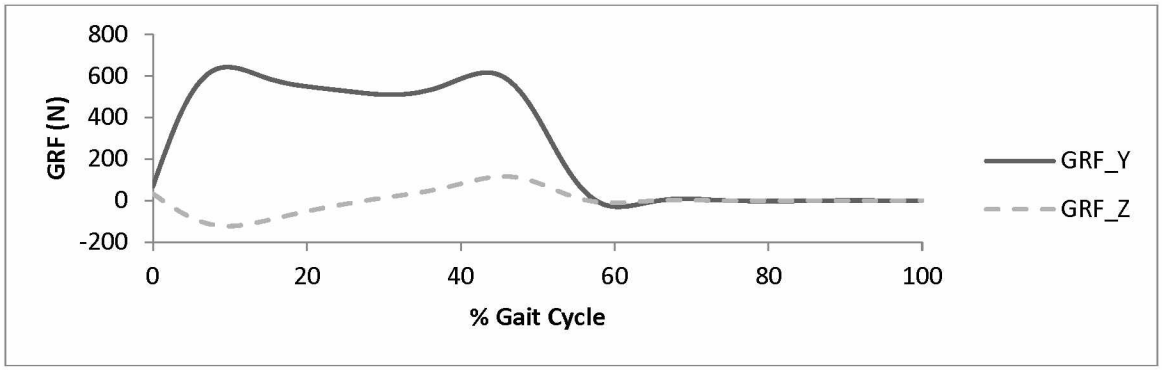

Figure 5.5 Ground reactive forces for 160 N carry at 1.2 m/s

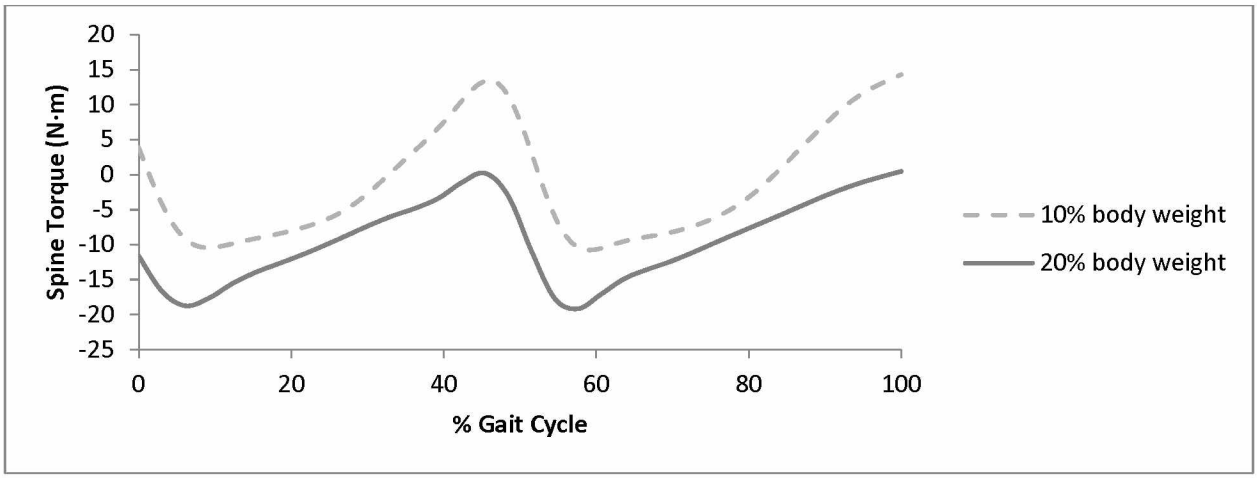

Figure 5.6 Spine torque at two different weights

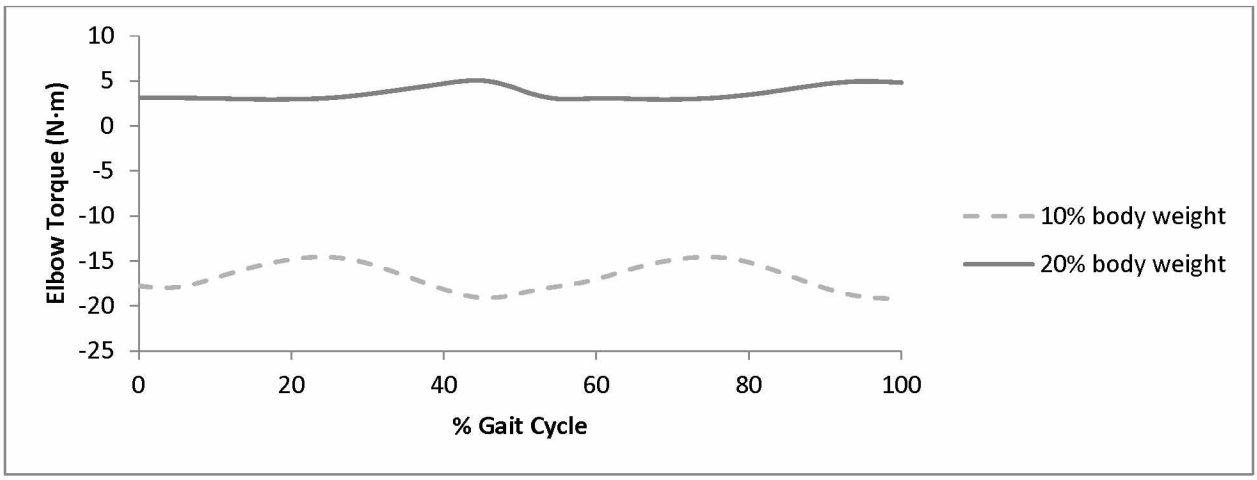

Figure 5.7 Elbow torque at two different weights

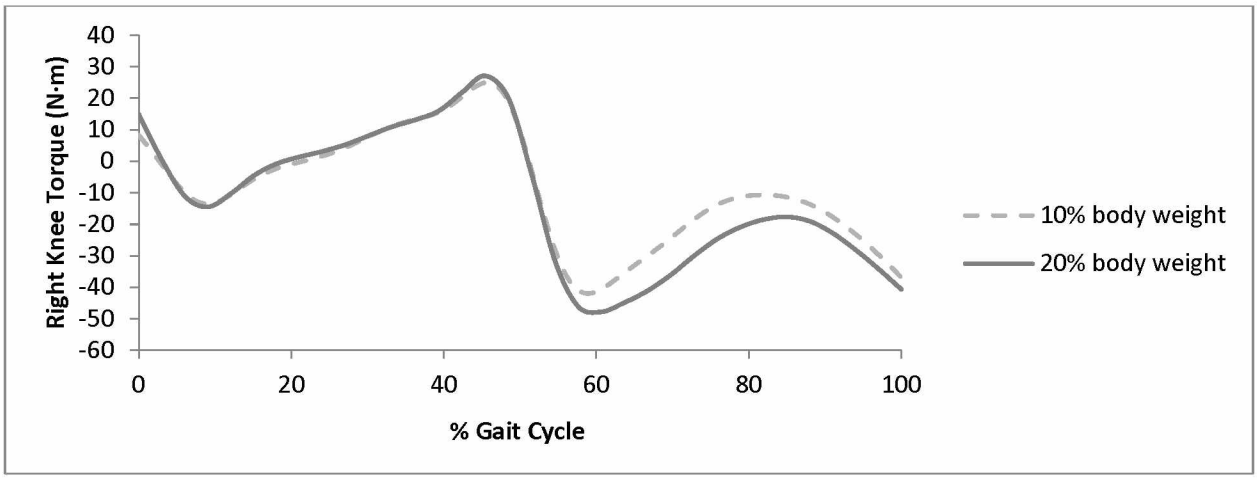

Figure 5.8 Right knee torque at two different weights

To further study cause-and-effect, increased walking speed is used in the simulation. The same

carrying task with the 10% bodyweight box weight is optimized, and the optimal carrying motion is obtained in Figure 5.9 and 5.10. Figure 5.9 depicts the motion where the weight is held at 80 N, but the speed is reduced to 1 m/s. Figure 5.10 shows the motion where weight is kept at 80 N, but the speed is increased to 1.4 m/s. GRF and joint torque profiles obtained from the motion prediction are shown in Figures 5.11 through 5.15.

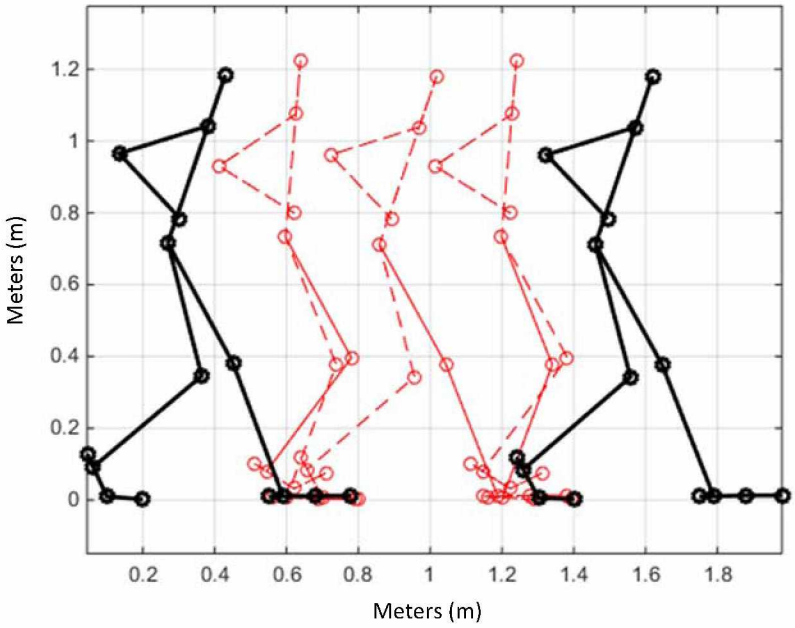

Figure 5.9 Optimal carrying motion for 80 N carry at 1.0 m/s

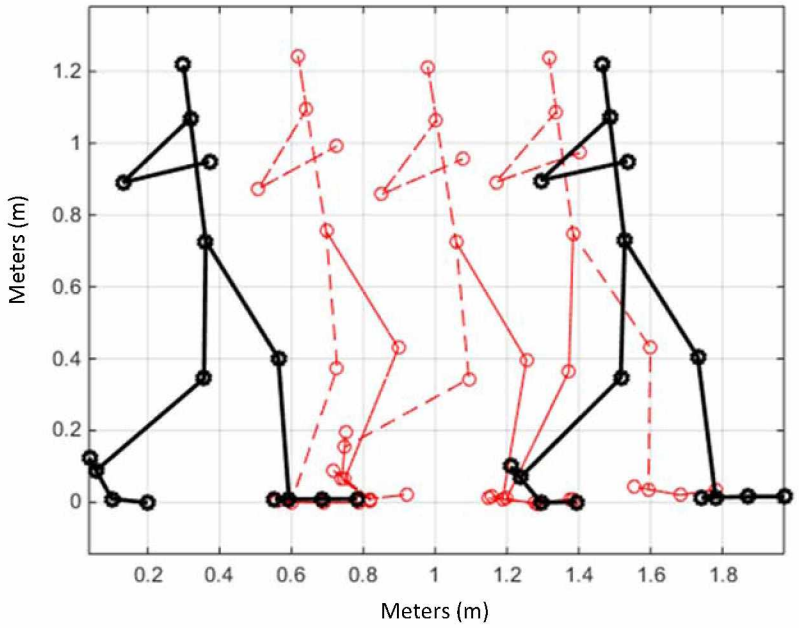

Figure 5.10 Optimal carrying motion for 80 N carry at 1.4 m/s

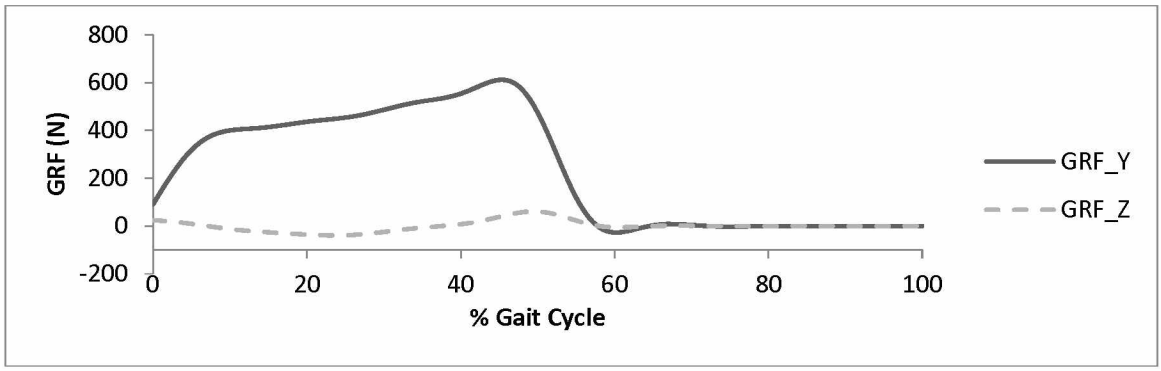

Figure 5.11 Ground reactive forces for 80 N carry at 1.0 m/s

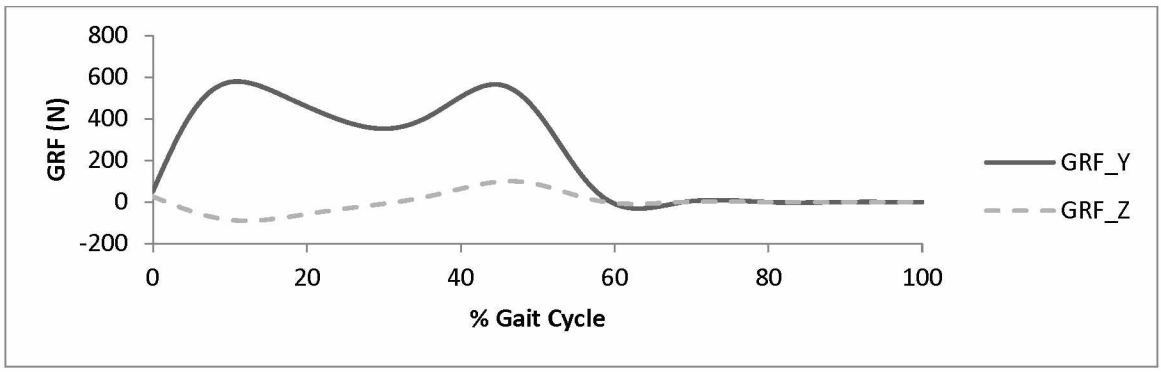

Figure 5.12 Ground reactive forces for 80 N carry at 1.4 m/s

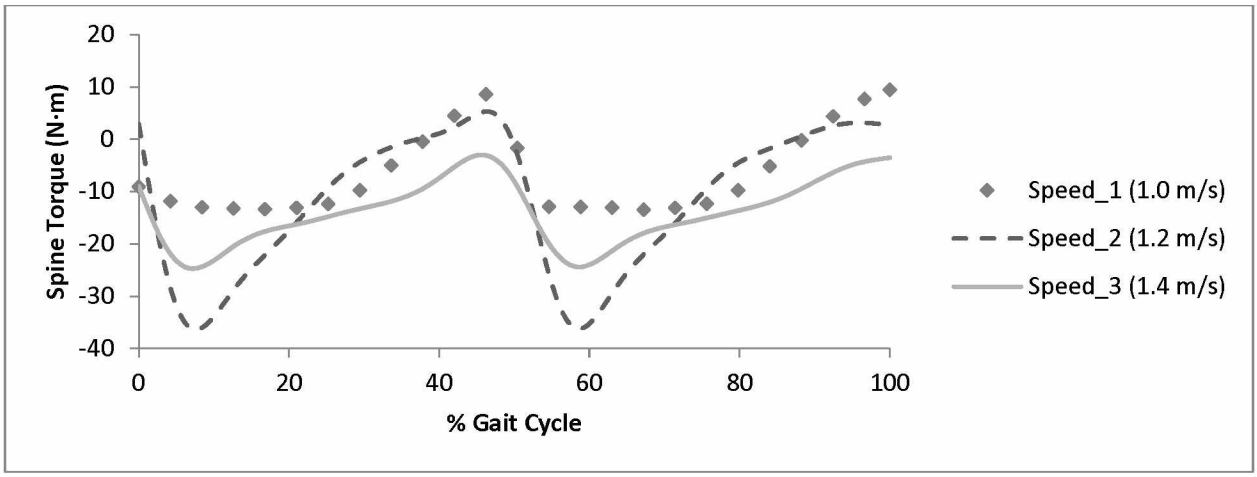

Figure 5.13 Spine torque at three different speeds

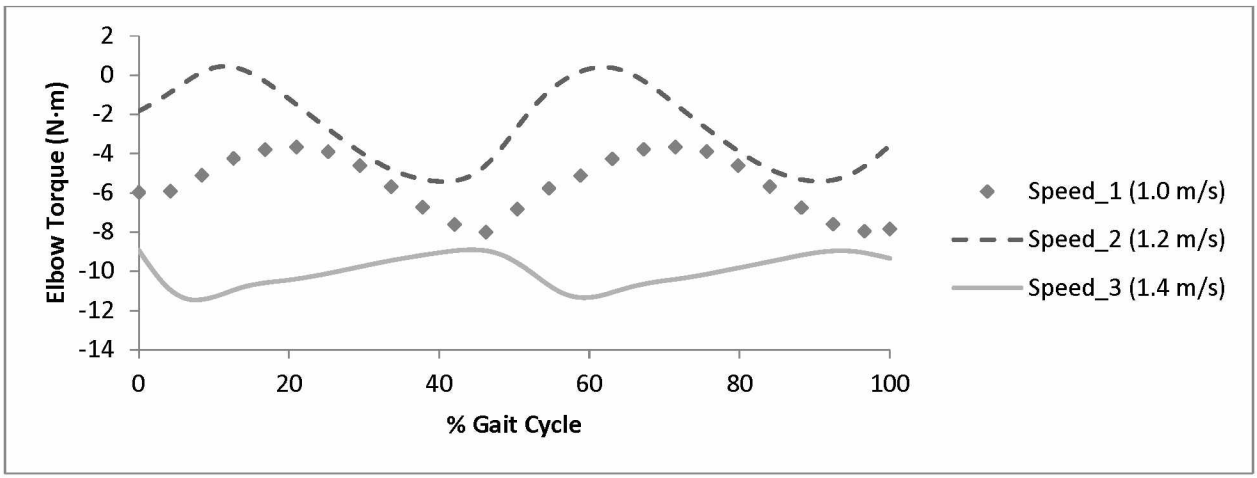

Figure 5.14 Elbow torque at three different speeds

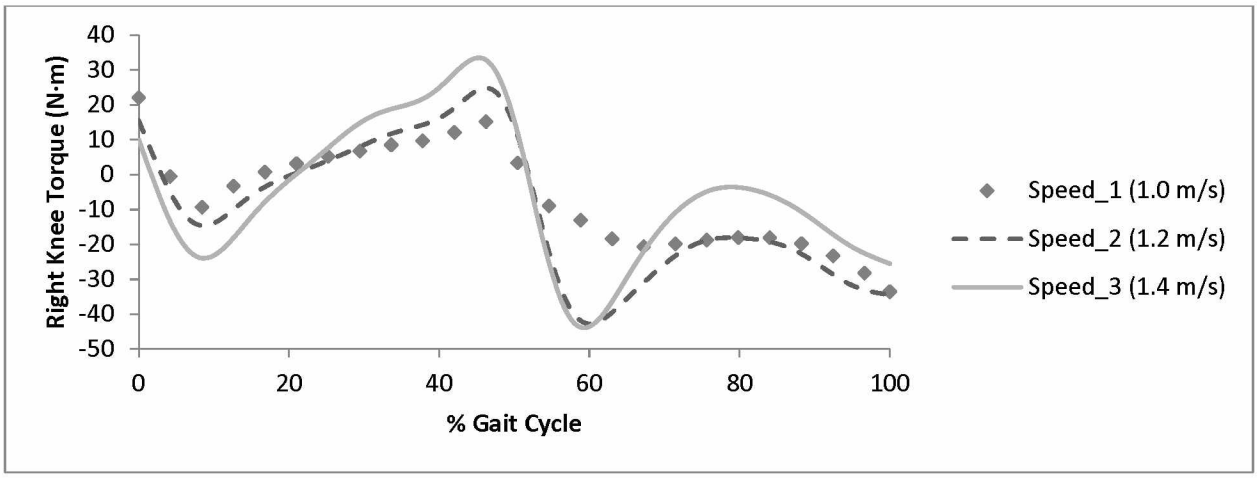

Figure 5.15 Right knee torque at three different speeds

5.3 Discussion

Comparing the data to the published work of Xiang et al. [18], the graphs of the GRF of varied weight follow the same general trend. Additionally, the graph of the joint torques of the right knee follows the same general trend as in the literature [18]. Given the similarities in trends, it can be empirically determined that the simulated data are sound.

Analyzing the figures regarding GRF, there is a portion of the figure that is zero. This is because the graph represents only one foot, so there is a portion in the gait cycle where the foot is in the air, and thus is experiencing zero GRF. Comparing the GRF figures for both the two different weights and three different speeds, it is evident that during carrying the variance in speed will have greater impact, leading to greater variance throughout the foot strike.

Looking first at the motion diagrams, the most noticeable difference is how the body holds the weight, evident in the position of the lower arm. As the body is imparted with a more difficult task, either from increased the weight or speed, we find that the joint angle of the spine in held at a more neutral angle. When the speed or weight is lowered, the spine is able to move more to provide "give" in the system, reducing the overall joint torque in subsequent joints such as the elbow. Variance of joint torque in the knee joint is minimal as evident in the figures.

It is evident that the elbow experiences the greatest variance in joint torque and location from the variety of given input parameters. This is most likely due to its ability of compensate for the other joints. Humans have much more control over their upper limbs for carrying versus spinal and lower limbs, and thus have a predisposition to repositioning their arms over spine and knee posture.

Chapter 6 Delivering Simulation

In this chapter, a complete delivering task is simulated by connecting the lifting and carrying together by a transition task. The transition task is formulated as a nonlinear optimization problem. A program based on a sequential quadratic programming (SQP) approach is used to solve the optimization problem. In addition to the kinematics data, kinetics data such as joint torques and ground reaction forces are recovered from the simulation.

6.1 Transition Simulation

6.1.1 Optimization Formulation

For the task of transitioning from lifting to carrying, the real task is transitioning from standing with two feet planted to walking on one foot until a carrying cycle is reached. For the given transition step length L, initial and final boundary joint angles and velocities, the motion and time duration are obtained using optimization.

Design Variables

The design variables are the joint angle profiles and time duration: $\mathbf{q(t)}$, T.

Objective Function

The goal at this stage is to determine the best way to minimize the dynamic effort and the joint angle discomfort, which is calculated by minimizing the following objective function:

$$F(q) = c_e \sum_{i=3}^{n} \int_{t=0}^{T} \left(\frac{\tau_i(q)}{\tau_i(q)^U - \tau_i(q)^L}\right)^2 dt + c_j \sum_{i=3}^{n} \int_{t=0}^{T} \left(\frac{q_i - \hat{q}_i}{q_i{}^U - q_i{}^L}\right)^2 dt \qquad (6.1)$$

where n is the number of degrees of freedom, T is the total time, τ_i^U is the upper torque limit for ith joint, τ_i^L is the lower torque limit, $q_i{}^U$ is the upper joint limit, $q_i{}^L$ is the lower joint limit, $\hat{q}_i$ is the average of the ith initial and final boundary joint angle values, c_e is the coefficient for the dynamic effort function, and c_j is the coefficient for the joint angle discomfort function. From SNOPT [10], it is determined that there are

86 variables to be optimized.

Constraints

The constraints include: (1) joint angle limits, (2) torque limits, (3) foot contacting position, (4) foot-ground penetration, (5) dynamic stability, (6) body collision avoidance, (7) ground clearance, and (8) boundary conditions at the beginning and ending of the transition to connect the previous lifting motion to the following carrying motion. From SNOPT [10], it is determined that there are 526 total nonlinear constraints.

6.1.2 Results

In this simulation, the step length is specified for a transitionary task. Given the box weight, the dynamic transitionary motion and total time are predicted to minimize the performance measure, dynamic effort and joint discomfort, and subject to physical constraints. The initial posture and velocity of the figure is obtained from the final posture and velocity after lifting. Figure 6.1 shows the resulting optimal transitionary motion.

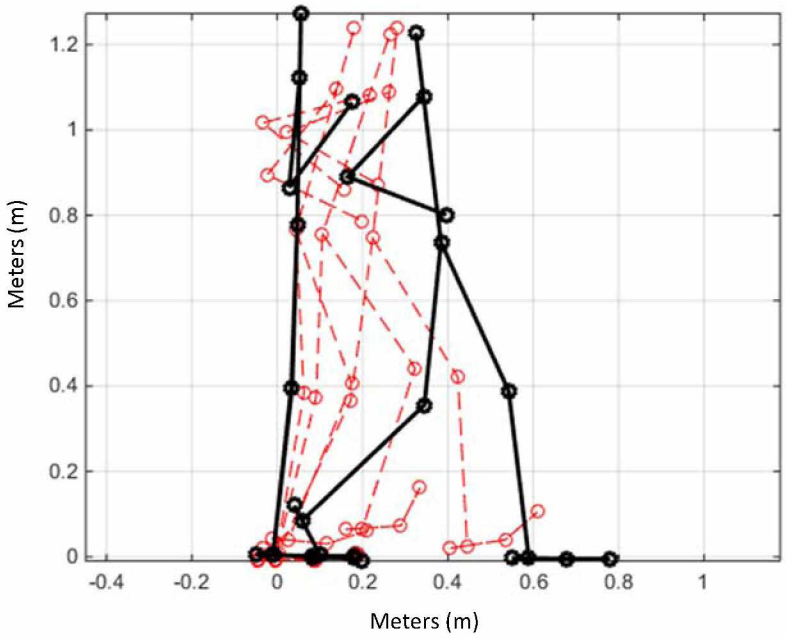

Figure 6.1 Optimal transition motion at 80 N

6.2 Delivering Simulation

6.2.1 Formulation

For the delivery simulation, the two previous motions (lifting and carrying) were stitched together using transition tasks to make one complete delivery task. A complete delivery task consists of five parts as follows: (1) an initial lifting, (2) the transition from the lifted posture to a walking carrying gait, (3) a carrying component, (4) the transition of stopping back to a standing posture, and (5) final delivering by either lifting the package higher or placing on a surface lower than the current state.

For the optimization of the components, the initial and final postures and velocities of the lifting and carrying tasks were inserted into the transition code to make a seamless delivery motion. To go about running all the codes in the specific sequence, a batch script was written instead of re-writing new code as a sum of the three. The advantages of using a batch script instead of writing new code are twofold: first and foremost to save the time that would be spent to write and debug new code, and second to keep the sections separate in the case that adjustments needed to be made.

The batch script runs as follows:

1. Call lifting and carrying code.
2. Copy specific files from their respective folders to a local folder for later use.
3. Call the transition code with the initial and final postures and velocities taken from the lifting and carrying code.
4. Copy specific files for later use.
5. Call lifting code for the back half of the delivery task.
6. Copy specific files from their respective folders for later use.
7. Call the transition code with the initial and final positions taken from the second lifting and carrying code.
8. Copy specific files for later use.

9. Using the copied files of data, stitch them all together in MATLAB to make larger data files of the whole delivery motion, in the order previously mentioned.
10. Using similar code from the previous tasks to determine all of the desired graphs: Joint torque, joint angle, GRF, and a graph of the optimized motion.

The image below presents a flow chart depicting the batch script:

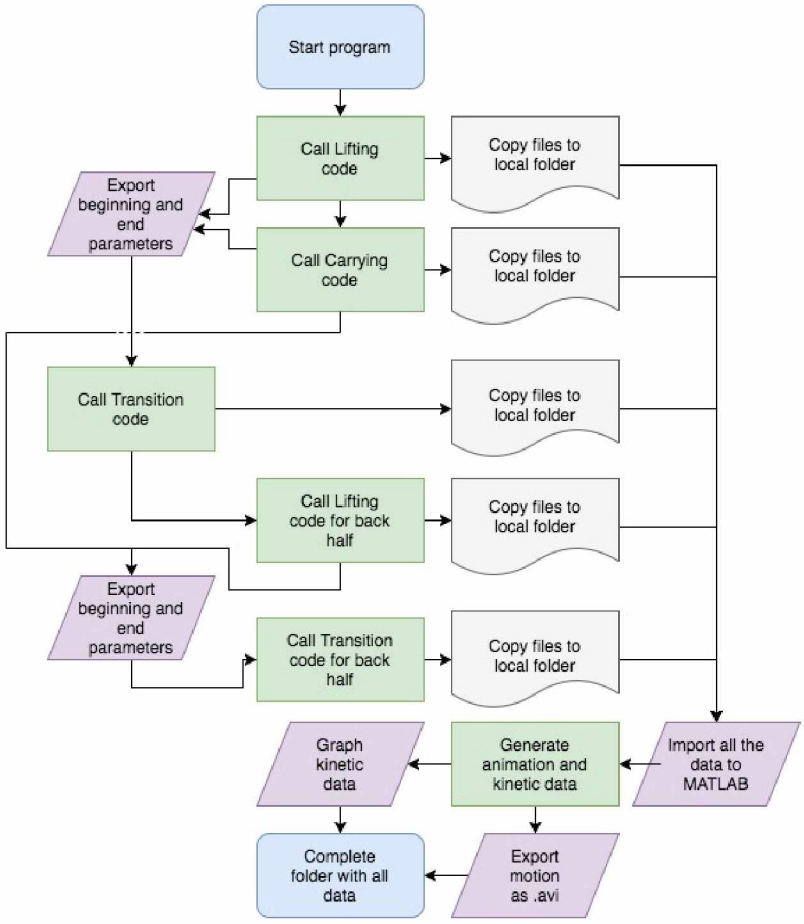

The significance of the batch script is the ability to cycle back data from the various tasks throughout the delivery motion. Therefore, having two code files for lifting and carrying, we can re-label the intermediate boundary data files, and input it back into the transition task; effectively reusing the same code and reducing the overall size. In addition, since the batch file calls the code from original folders each time, when adjustments need to be made, it is only in the original code.

6.2.2 Results

In this simulation, the total time is the normalized sum of the times from all five tasks. Given the variables that are initially input by the user, the delivery motion is predicted to minimize the performance measure, dynamic effort for lifting and carrying, and dynamic effort and joint discomfort for transition, and subject to physical constraints. Figure 6.2 shows the resulting optimal motion. The joint angle profiles are depicted in Figures 6.3 through 6.5, the first representing the joint angle of the elbow, the middle the knee, and the final the spine. For the graphical data, each graph is divided into five equal sections by vertical lines. These represent the separation between the various tasks in the order: lifting, transition, carrying, transition, unloading.

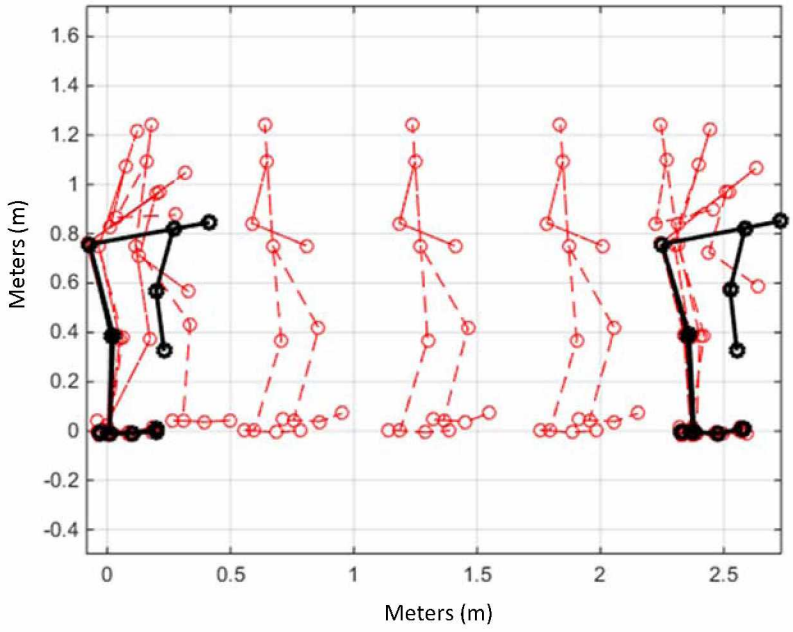

Figure 6.2 Optimal delivery motion for 80 N

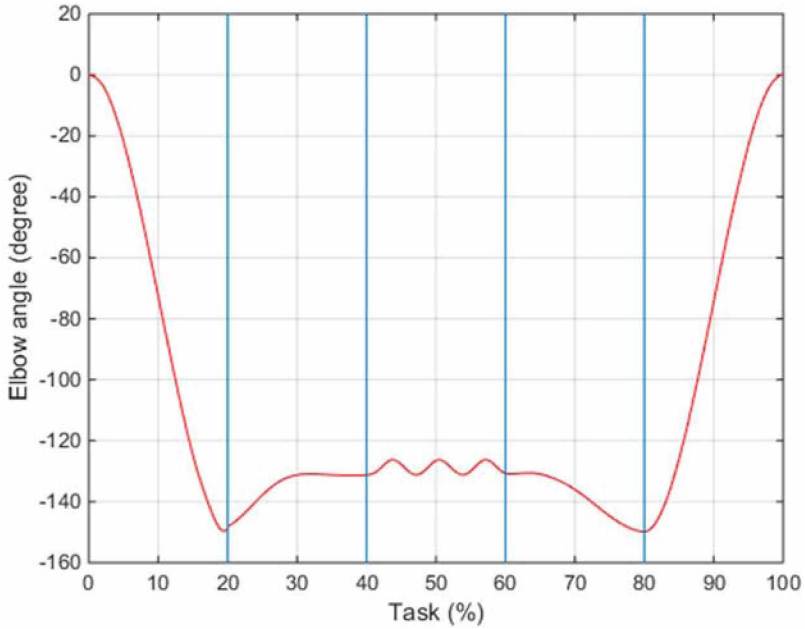

Figure 6.3 Joint angle of elbow over delivery motion

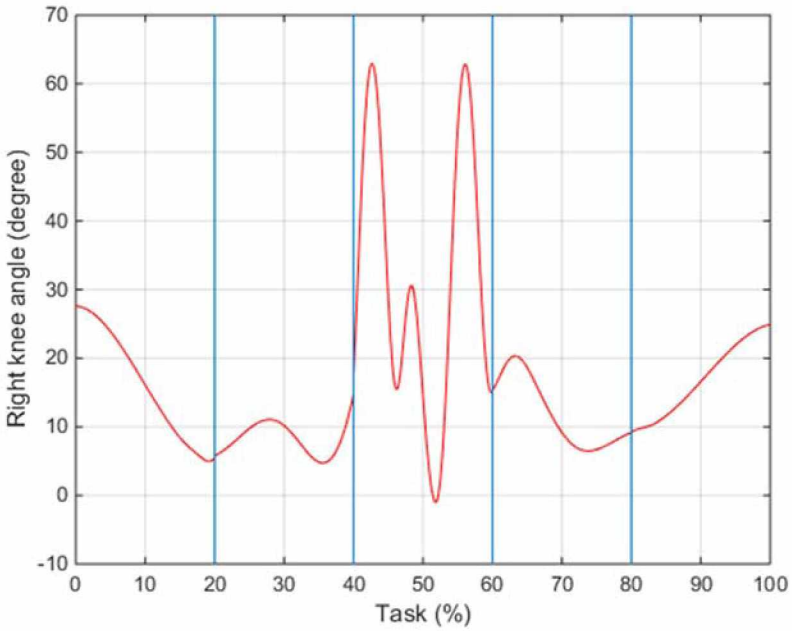

Figure 6.4 Joint angle of knee over delivery motion

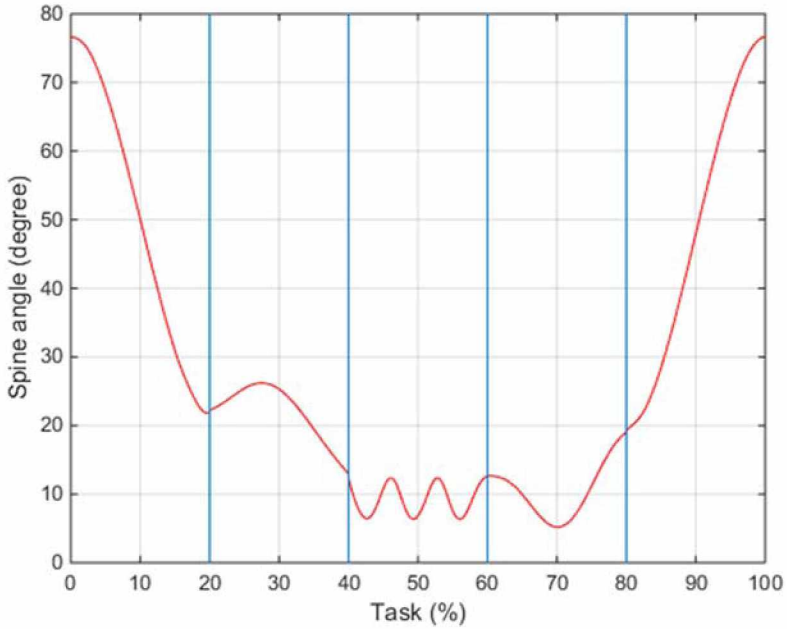

Figure 6.5 Joint angle of spine over deliver motion

To study the optimization, the joint torque profiles and the ground reactive forces are obtained from the motion optimization shown in Figures 6.6 through 6.12, respectively. Figures 6.6 through 6.8 depict the variance in the joint torques between the three points of interest: first elbow, second knee, and third knee. Figure 6.9 depicts the variance in the ground reactive forces for the left foot in the z-direction (vertical direction), while Figure 6.10 shows the GRF for the left foot in the y-direction (fore-aft direction). Figure 6.11 is the GRF of the right foot in the z-direction, and 6.12 the right foot in the y-direction.

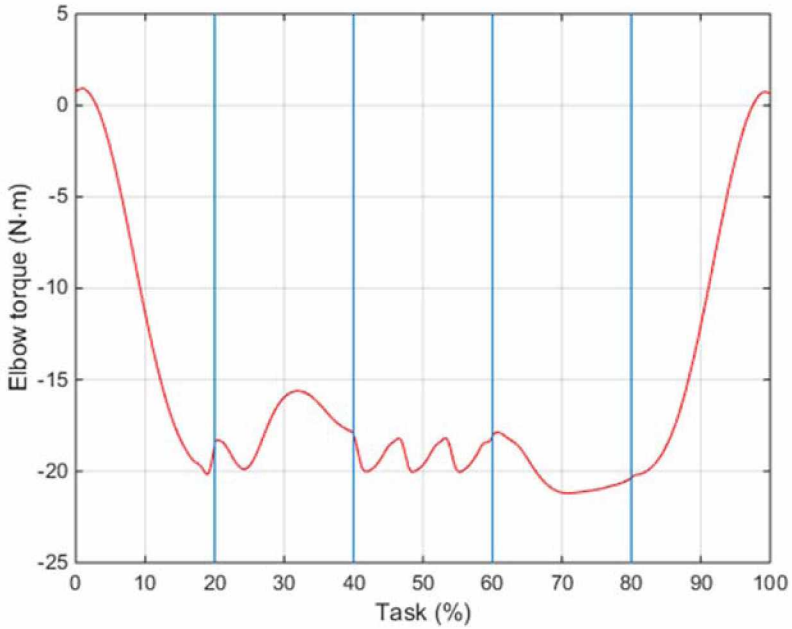

Figure 6.6 Joint torque in the elbow over the delivery motion

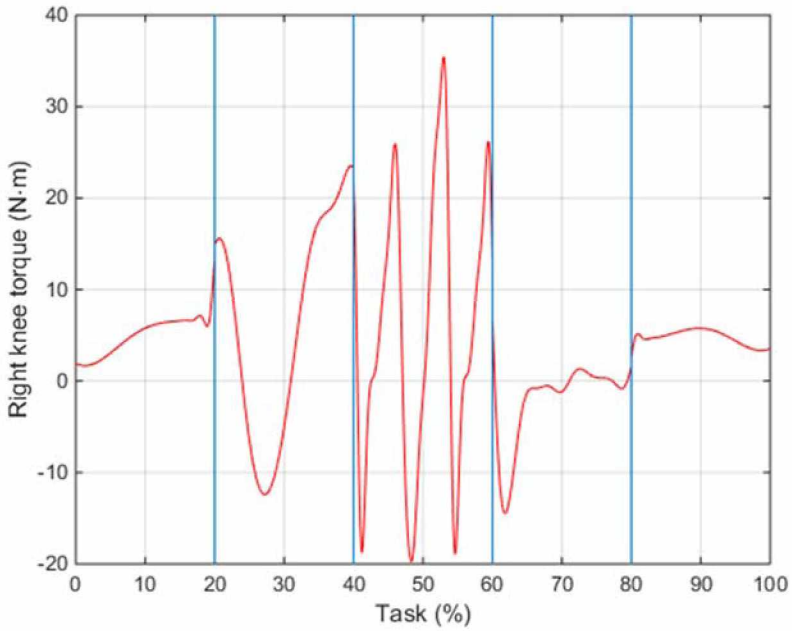

Figure 6.7 Joint torque in knee over deliver motion

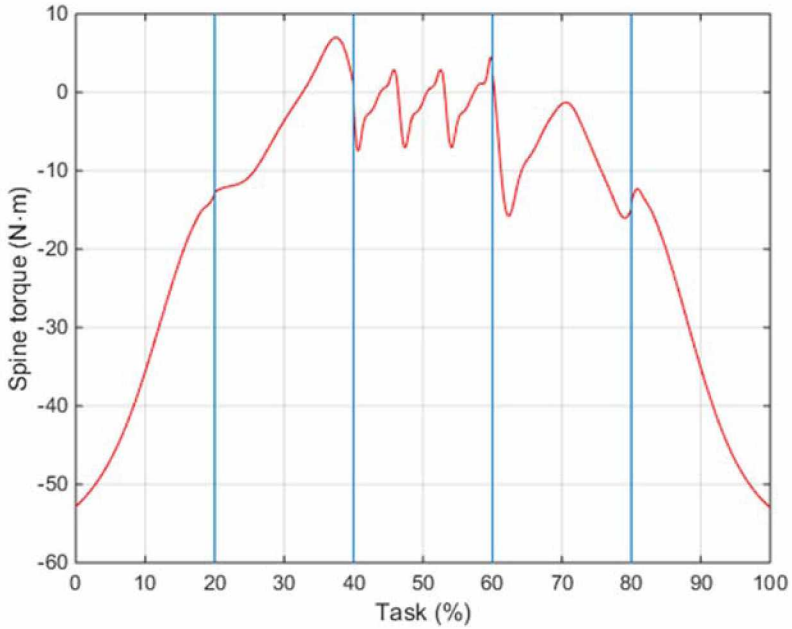

Figure 6.8 Joint torque of spine over the delivery motion

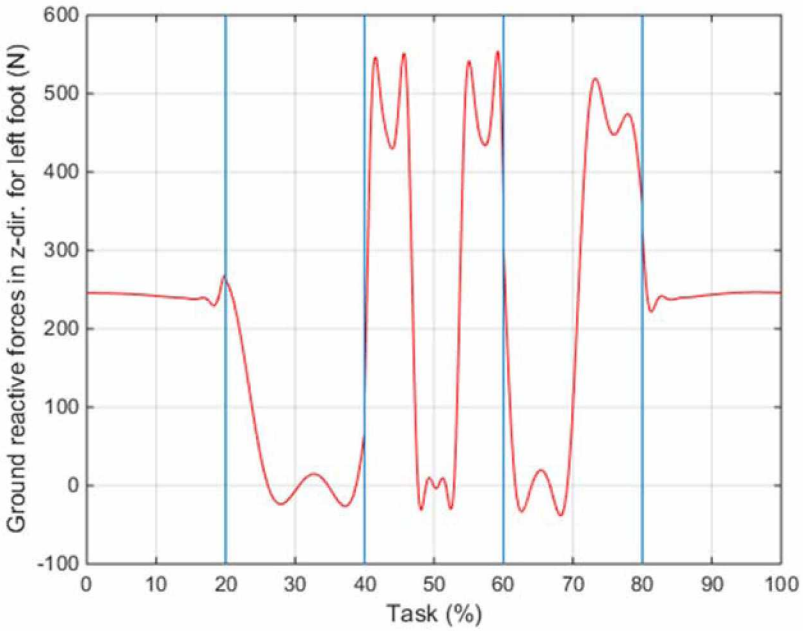

Figure 6.9 Ground reaction force in the z-direction for left foot

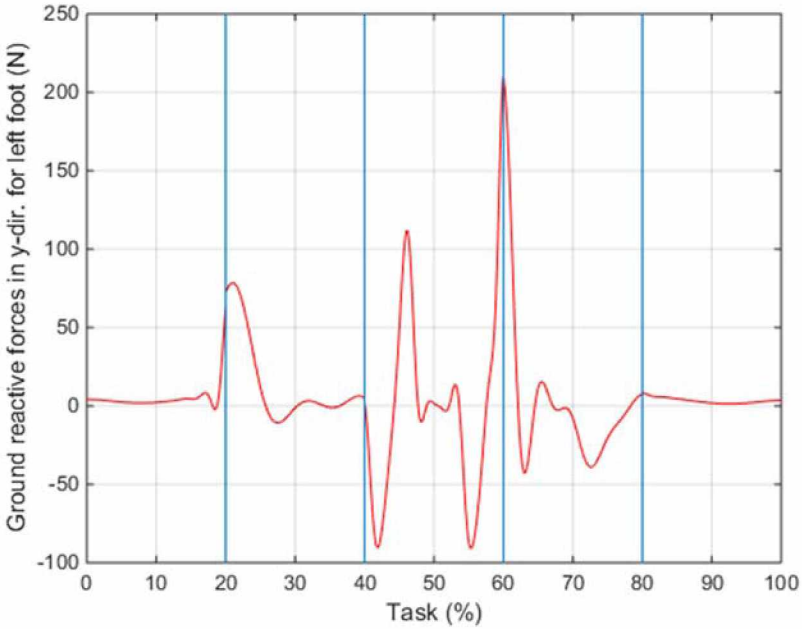

Figure 6.10 Ground reaction force in y-direction for left foot

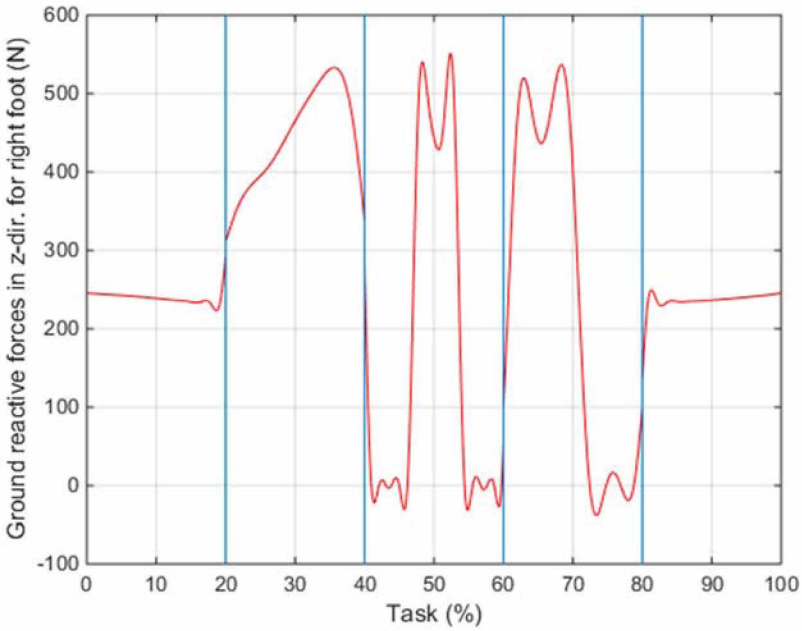

Figure 6.11 Ground reaction force in z-direction for right foot

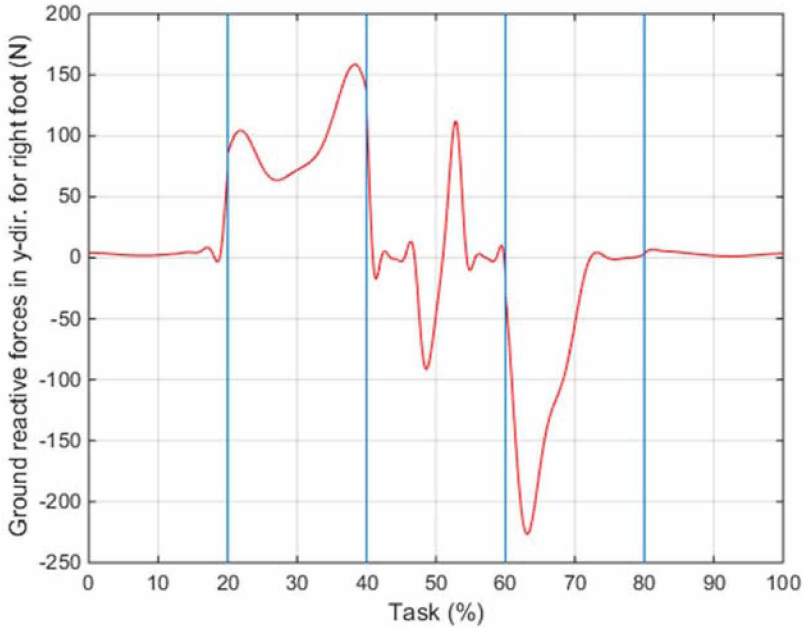

Figure 6.12 Ground reaction force for y-direction for right foot

6.2.3 Discussion

Analyzing the Figures 6.10 and 6.12 regarding GRF in y-direction, they both have zero relative change for the first and final 20% of the simulation. Note that the time is normalized so that each task represents 20% of the total graph. The relative zero change is because these parts of the graphs represent the lifting portion of the delivery motion where the box is moving vertically, thus the feet stay planted and are experiencing zero variance in y-direction GRF. There is the illusion of more activity in the middle of the graphs, but that is created by the normalization of the time components when stitching all of the graphs together. The real transition motion is a very small moment in time (less than a second). However, the middle portions do contain the most activity due to the walking dynamics, and thus exhibit the difference in force when compared to the other sections.

Analyzing the Figures 6.9 and 6.11 regarding GRF in z-direction, there is a portion of the graph that is zero. This is because the graph represents a portion in the gait cycle where the foot is in the air, and thus is experiencing zero GRF. Since we only simulate one step carrying motion, the second step will repeat the first step motion with swapping roles of right and left legs.

It is evident from the motion diagram in Figure 6.2 that the figure follows the expected trends for delivery. What stands out most is the lack of movement in the knees, most specifically during the lifting process. This suggests that it is more efficient to use the back to lift versus the knees for a weight of approximately 10% body weight. If the weight were to increase, it would follow the earlier trends (from the lifting section), where the knees play a larger role. Additionally, during the carrying section the spine in at a slight recline. This is most likely to enable the ability to pull the center of gravity above the hips without having to pull the package closer to the person, essentially hugging it, and making stability more of an issue. The graph also visually represents the separation of effort amongst the joints during the various stages of the delivery task, which will be elaborated more in the next paragraph.

For the joint torques in Figures 6.6 through 6.8, it seems that the joints of interest each have respective sections when they play a larger role more or less. The elbows stay active except for the middle portion when the figure is carrying, when the elbows lock. The spine has the most activity when lifting, when the body bends over to pick up the box, with a mirrored trend when putting the package back on the ground. Finally, the knees show the most activity when carrying, because they are doing a majority of the work during this portion. The trends from these three joints create a picture that the body performs most optimally when one joint is the predominately active one, and the others are more stagnant, versus a situation where the work is divided evenly amongst the joints. However, this is just a picture of the three described joints and is not a great representation since there are many more joints that might be playing crucial roles in the task. These joints are chosen since they have the highest impact during a full delivery task.

6.3 Validation

In this section, we use a camera to record a simple delivering motion with light weight box. We will only compare the simulation with the video qualitatively.

For the video comparison, we ran four people through a systematic test to generate images to compare the generated motion images. For the test, we used two different weights: 40 N and 80 N. Figure 6.13 shows the complete delivery motion for a 40 N delivery.

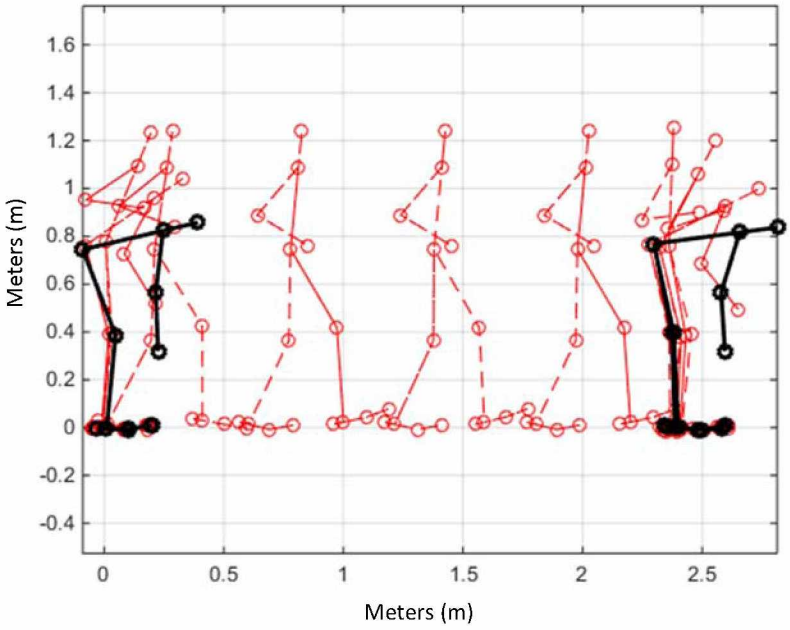

Figure 6.13 Optimal delivery motion for 40 N

It was very important that the subjects walk the same number of steps, and in the same order, for the sake of accurate comparison. The individuals were allowed to practice walking to get the process consistent. The parameters were as follows: fully stand up before beginning to walk, lead with their left foot, take three steps, end on their right foot. They were also asked segment their motions, so as to allow for better video capture for the comparison.

Each subject ran through both heavy and light delivery tasks multiple times. Below are runs from the subjects for both heavy (80 N) and light (40 N) weights. For illustration purposes in this study, Figures 6.14 through 6.21 show the process broken into consecutive images.

Figure 6.14 Subject one carrying 40 N

Figure 6.15 Subject one carrying 80 N

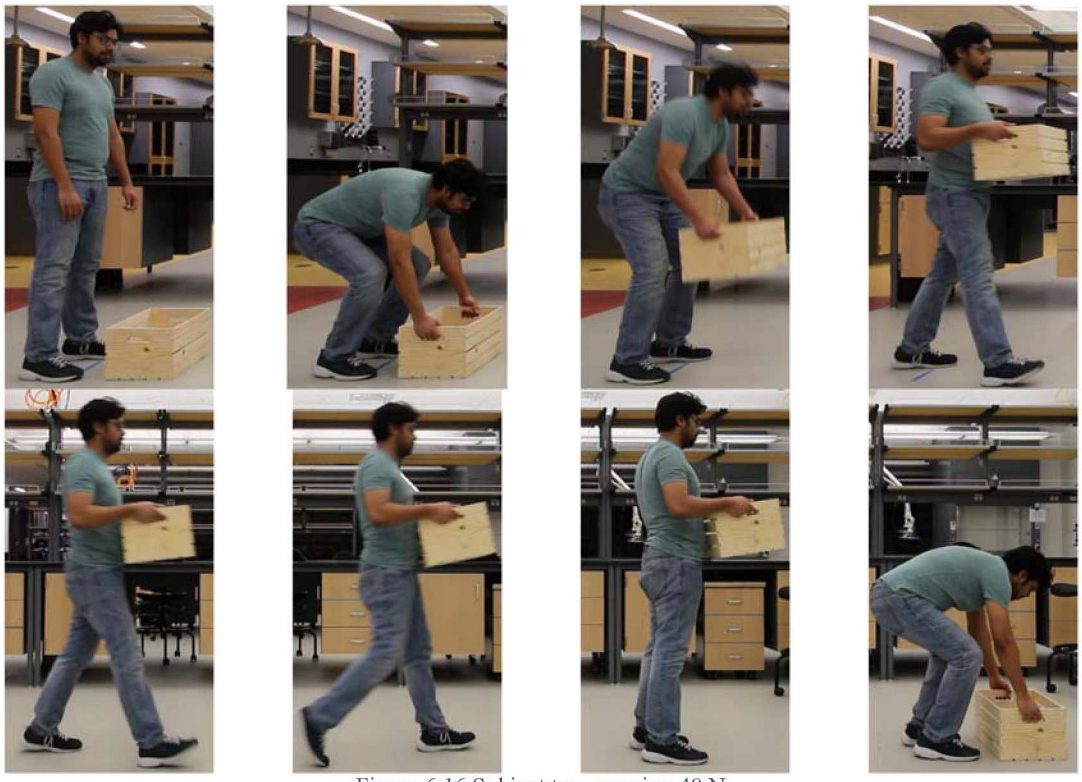

Figure 6.16 Subject two carrying 40 N

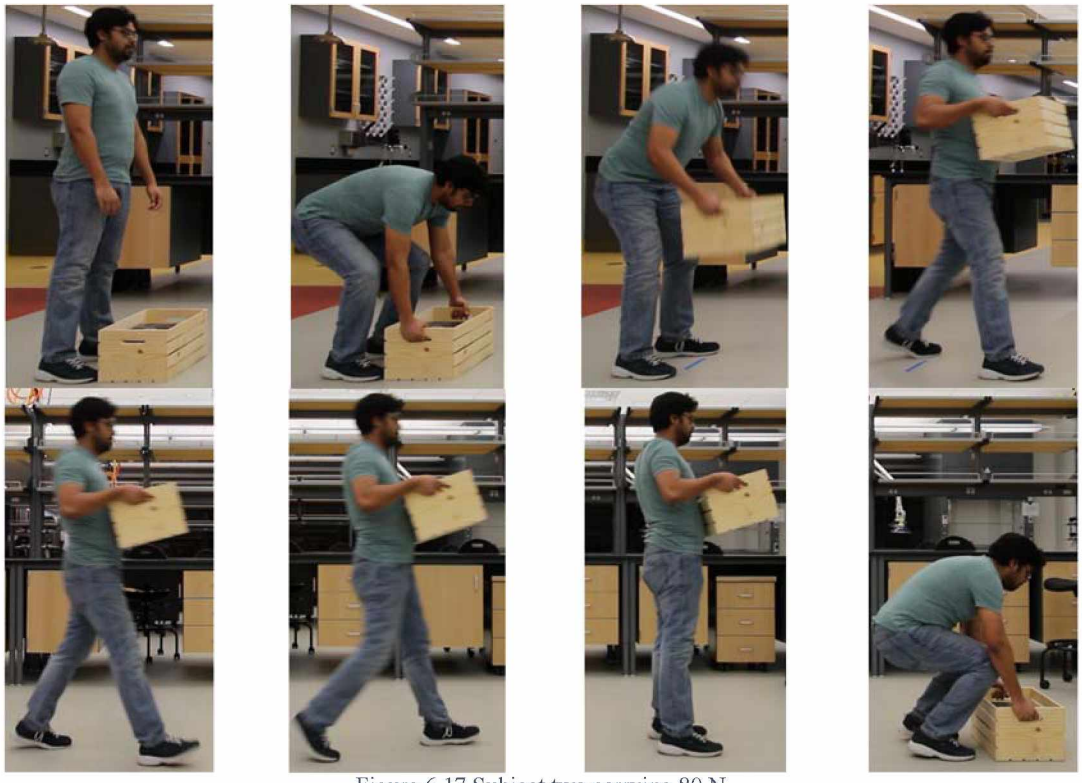

Figure 6.17 Subject two carrying 80 N

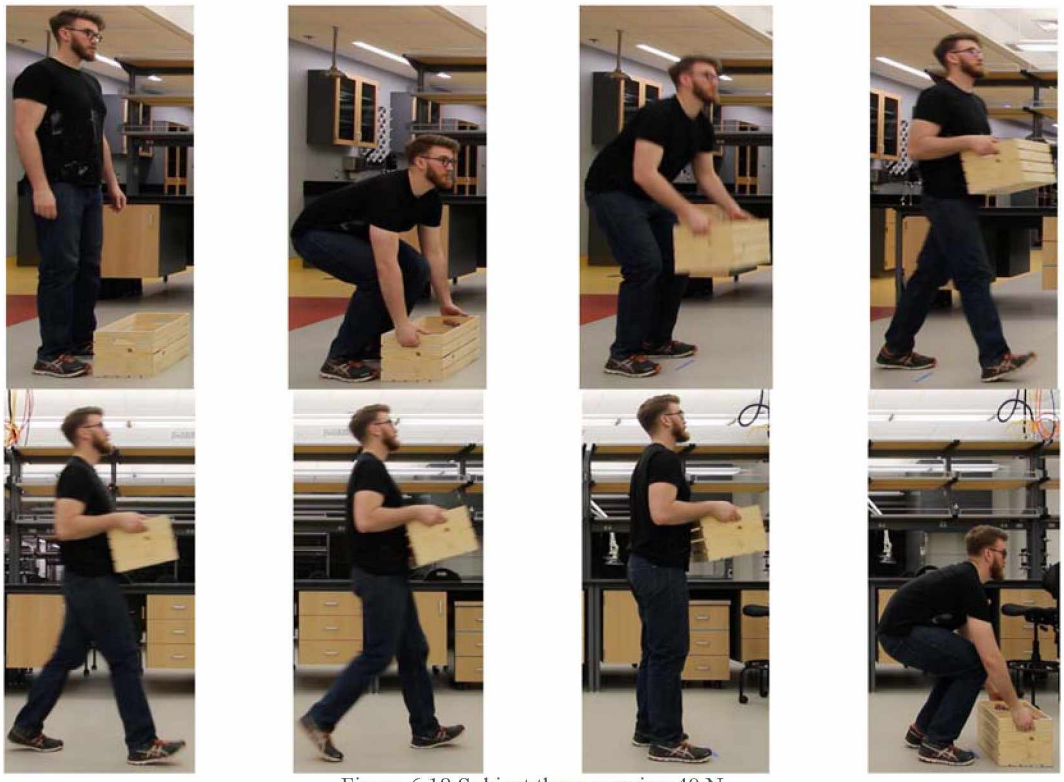

Figure 6.18 Subject three carrying 40 N

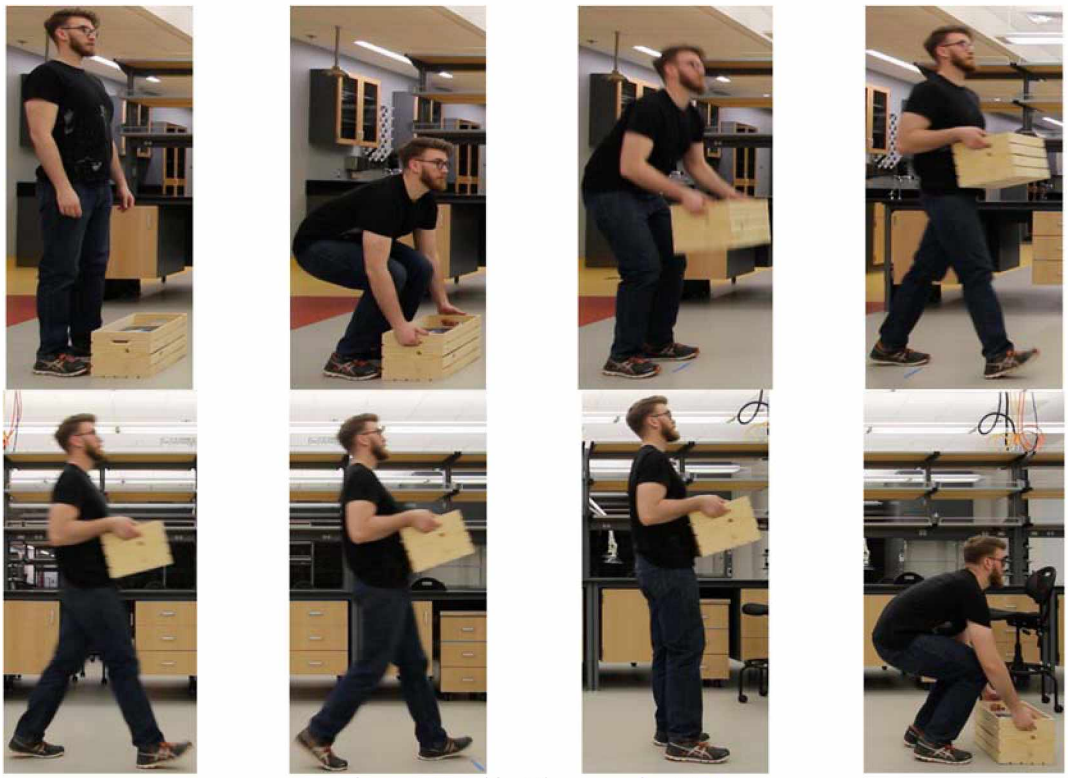

Figure 6.19 Subject three carrying 80 N

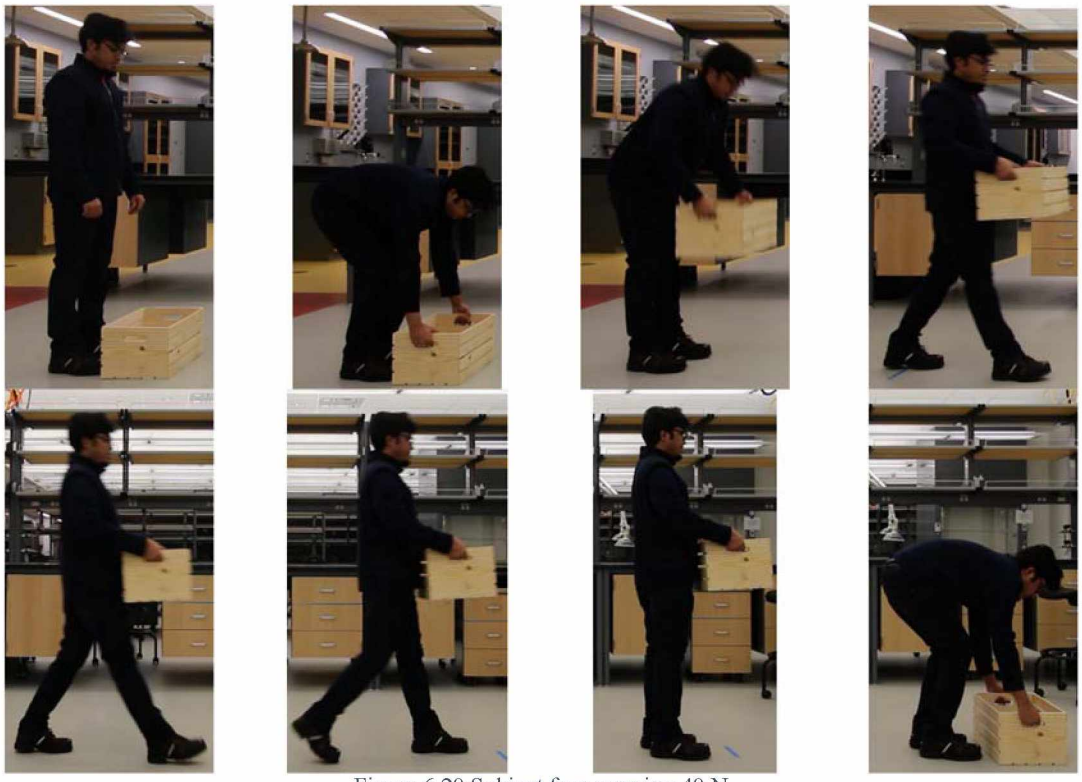

Figure 6.20 Subject four carrying 40 N

Figure 6.21 Subject four carrying 80 N

Use of Adobe Photoshop was attempted to create a single image much like in the generated image. However, since the subjects have substantially more surface area than a stick figure, the image became too crowded, rendering the image meaningless.

The greatest discovery from this experiment was how differently humans naturally gravitate to walking. Each subject had different tendencies that they gravitated to. For comparison sake, we worked on creating a systematic process to make sure everyone walked as similarly as possible.

Additional issues arose when it came to how high to lift the box. Most subjects naturally held the box lower, almost resting it on their thighs. The issue with this situation is that the box bounced off their legs as they walked. However, a parameter in the simulated delivery motion is to avoid colliding the box into the person. Therefore, it generates an image where the box is naturally held higher. To compensate for this, the subjects practiced walking where they consciously avoided bouncing the box. What resulted was the box being held higher on the person. The experimental snapshots Figures 6.14 through 6.21 show similar motion with the stick diagram simulation in Figure 6.13 except the last unloading phase. This is maybe because the unloading motion uses a different strategy from the lifting motion. However, in this study, we use same optimization formulations for lifting and unloading motions.

A similarity between the generated motion and the experimental data is how the figures walk to stay balanced. Since it's only two dimensional, the ability to balance relies on moving the torso to compensate for more or less weight, so as to move the center of mass above the hips. In Figures 6.15-6.19 (only odd), there is a trend of leaning back when walking with the box, very similar to the position of the stick diagram as it walks with the heavier load. In conclusion, the qualitative comparison validates the motion optimization generated.

A difference to note between the simulation and validation is the simplification in the decision making process. While the transition is optimized from the lifting and carrying tasks, as humans there is not that foresight, and adjustments are made on the spot. In addition, the subjects had a proclivity to drop the box, where as the simulation had a smooth unloading process.

Chapter 7 Conclusion and Future Research

7.1 Conclusion

In this thesis, an accurate 2D skeletal model was developed to predict and analyze the dynamics of human box delivery motion. Breaking apart the system into a multistage approach, the complete delivery motion is determined. Forward kinematics and backward dynamics are used to build equations of motions. A SQP-based algorithm was used to solve the optimization problem with performance measures and constraints. The Denavit-Hartenberg [6] method was used to reference the information of parent and sibling joints. The goal is to minimize the effort level, which is the sum of the integral of the torques squared.

Breaking the motion into three parts, it is easier to analyze what is happening at the pivotal moments of the delivery motion. It is also computationally efficient to simulate three parts separately. Here we can analyze the joint angles, joint torques, and the ground reactive forces both piecewise, and all stitched together. To stich all the components together, I used a batch script so that I could reintegrate the exported data from the files back into the files without having to create additional code, cutting down on the bloat of the system.

Finally, the model simulation was compared to actual people delivering a box. From the photos we can see similarities between them. The significance of this comparison was to see the effectiveness of the model through a qualitative validation.

7.2 Future Research

There is the possibility to continue in dynamics as well as its expansion into biomechanics. Below are just a few subjects which can use this research as a stepping off point.

1. Anthropometric data

The foundation of this research is based significantly on tabulated values. The accuracy of these values is pivotal to this model. Ergo, as continued research into anthropometric data continues, this model

can be continually refined and improved. Currently, it is difficult to isolate the physical joints in research, however as the significance of joint health continues to be a priority, the advancements in the field continue.

2. 3D Model

The most immediate continuation of this research would be to expand it to a 3D model. The progression to a 3D model would spike the complexity due to its expansion of both DOF on each joint, but also adding a whole new axis of movement (depth).

3. Musculoskeletal model

Currently this model only takes into account the individual joints. With tabulated values of the limitations of the joints from the muscles, the problem is significantly simplified. This leads to a more robust system that is easier to compute. The optimization of a musculoskeletal model would be very burdensome in comparison, however yield a more accurate result. Possible ways to incorporate muscle into the system would be to break everything down to individual muscles. Piece by piece analyze the relations, and then build a model up from there.

4. Physical Applications

With a better understanding of where forces are being applied on the skeleton for simple tasks, physical contraptions can be made to aid. Already, companies are looking into way to prevent injuries by making exoskeleton-like systems to reinforce weaker areas of the body. By better understanding what joints take the most stain from repeated tasks, such as a luggage handler for an airline company, companies know where to invest resources into research.

5. Motion Capture Validation

More rigorous validations based on motion capture data will be pursued for this research.

Chapter 8 Reference

[1] Anderson, F. C. and Pandy, M. G. (2001). "Dynamic optimization of human walking." Journal of Biomechanical Engineering 123(5): 381-390.

[2] Bessonnet, G., et al. (2004). "Optimal gait synthesis of a seven-link planar biped." The International Journal of Robotics Research 23(10-11): 1059-1073.

[3] Cheng, H., Obergefell, L., Rizer, A. (1994). "Generator of body (GEBOD) manual, AL.CF-TR-1994-0051." Armstrong Laboratory, Wright-Patterson Air Force Base, OH.

[4] Chevallereau, C. and Aoustin, Y. (2001). "Optimal reference trajectories for walking and running of a biped robot." Robotica 19(5): 557-569.

[5] Chung, H. J., et al. (2016). "A method of optimization based human dynamic simulation for exoskeleton robot design and assessment." 2016 13th International Conference on Ubiquitous Robots and Ambient Intelligence (URAI).

[6] Denavit, J. and Hartenberg, R.S. (1955). "A kinematic notation for lower pair mechanisms based on matrices." Journal of Applied Mechanics 22: 215-221

[7] Dysart, M. J. and Woldstad, J. C. (1996). "Posture prediction for static sagittal-plane lifting." Journal of biomechanics 29(10): 1393-1397.

[8] Eberhard, P. and Schiehlen, W. (2005). "Computational dynamics of multibody systems: history, formalisms, and applications." Journal of Computational and Nonlinear Dynamics 1(1): 3-12.

[9] Gazula, H., et al. (2015). "Using mutual information to capture major concerns of postural control in a tossing activity." Journal of Biomechanics 48(6): 1105-1111.

[10] Gill, P.E., Murray, W., Saunders, M.A. (2002). "SNOPT: an SQP algorithm for large-scale constrained optimization." Journal of Optimization 12(4): 979-1006.

[11] Hsiang, S. M. and McGorry, R. W. (1997). "Three different lifting strategies for controlling the motion patterns of the external load." Ergonomics 40(9): 928-939.

[12] Jomoah, I. M. (2014). "Biomechanical analysis of manual lifting tasks." Asian Transactions on Basic and Applied Sciences 4(2): 11.

[13] Leylavi Shoushtari, A. and Abedi, P. (2012). "Modelling and simulation of human-like movements for humanoid robots."

[14] Noone, G. and Mazumdar, J. (1992). "Lifting low-lying loads in the sagittal plane." Ergonomics 35(1): 65-92.

[15] Rostami, M. and Bessonnet, G. (1998). "Impactless sagittal gait of a biped robot during the single support phase." Proceedings. 1998 IEEE International Conference on Robotics and Automation (Cat. No.98CH36146).

[16] Sardain, P. and Bessonnet, G. (2004). "Forces acting on a biped robot. Center of pressure-zero moment point." IEEE Transactions on Systems, Man, and Cybernetics - Part A: Systems and Humans 34(5): 630-637.

[17] Winter, D. A. (1995). "Human balance and posture control during standing and walking."

[18] Xiang, Y. (2014). "Human carrying simulation with symmetric and asymmetric loads using optimization." J Appl Biomech 30(1): 140-146.

[19] Xiang, Y., et al. (2012). "3D human lifting motion prediction with different performance measures." International Journal of Humanoid Robotics 09(02): 1250012.

[20] Xiang, Y., et al. (2011). "Predictive simulation of human walking transitions using an optimization formulation." Structural and Multidisciplinary Optimization 45(5): 759-772.

[21] Xiang, Y., et al. (2010). "Human lifting simulation using a multi-objective optimization approach." Multibody System Dynamics 23(4): 431-451.